

# NAVAL POSTGRADUATE SCHOOL

## Monterey, California



## THESIS

### EVOLUTION OF BEDFORMS ON THE INNER-SHELF

by

Damon Beecher Dixon

September 2000

Thesis Co-Advisors:

Edward B. Thornton  
Timothy P. Stanton

Approved for public release; distribution is unlimited.

DTIC QUALITY INSPECTED 4

20001102 142

# REPORT DOCUMENTATION PAGE

Form Approved  
OMB No. 0704-0188

Public reporting burden for this collection of information is estimated to average 1 hour per response, including the time for reviewing instruction, searching existing data sources, gathering and maintaining the data needed, and completing and reviewing the collection of information. Send comments regarding this burden estimate or any other aspect of this collection of information, including suggestions for reducing this burden, to Washington headquarters Services, Directorate for Information Operations and Reports, 1215 Jefferson Davis Highway, Suite 1204, Arlington, VA 22202-4302, and to the Office of Management and Budget, Paperwork Reduction Project (0704-0188) Washington DC 20503.

1. AGENCY USE ONLY  
(Leave blank)

2. REPORT DATE  
September 2000

3. REPORT TYPE AND DATES COVERED  
Master's Thesis

4. TITLE AND SUBTITLE  
Evolution of Bedforms on the Inner-shelf

5. FUNDING NUMBERS

6. AUTHOR(S)  
Dixon, Damon Beecher

7. PERFORMING ORGANIZATION NAME(S) AND ADDRESS(ES)  
Naval Postgraduate School  
Monterey, CA 93943-5000

8. PERFORMING ORGANIZATION  
REPORT NUMBER

9. SPONSORING / MONITORING AGENCY NAME(S) AND ADDRESS(ES)  
Office of Naval Research  
Coastal Sciences  
800 North Quincy Street  
Arlington, VA 22217

10. SPONSORING / MONITORING  
AGENCY REPORT NUMBER

## 11. SUPPLEMENTARY NOTES

The views expressed in this thesis are those of the author and do not reflect the official policy or position of the Department of Defense or the U.S. Government.

12a. DISTRIBUTION / AVAILABILITY STATEMENT  
Approved for public release; distribution is unlimited.

12b. DISTRIBUTION CODE

## 13. ABSTRACT (maxi mum 200 words)

Observations of the temporal evolution of the wave-formed ripples are analyzed in terms of geometric properties. Three weeks of bedform observations were obtained using underwater video of a sheet of laser light projected on the bed at the Monterey Bay Inner Shelf Observatory in thirteen-meter depth water. The bed consists of fine sand (mean grain size 0.12mm). Low to moderate narrow-band swell waves occurred during the observation period. Ripple geometry consisted of orbital and suborbital vortex wave ripples, and relic ripples left after larger wave events. The bedforms generally changed size and shape when the grain roughness Shields parameter exceeded a critical value of 0.04. Ripple migration was offshore at rates of 2-10 cm/day during active sediment transport events. Skewness of velocities (low and high passed) were calculated to explain offshore ripple migration, but showed no preferred direction. Mean currents were weak. Significant positive (offshore) correlation was obtained between the short-wave envelope and infragravity waves indicating wave-group forced bound long waves (surf beat) combined with stirring by the short waves might explain the offshore sediment transport and ripple migration.

14. SUBJECT TERMS  
Ripples, Sediment Transport, Shields Parameter, Bound Long Waves

15. NUMBER OF  
PAGES  
61

16. PRICE CODE

17. SECURITY  
CLASSIFICATIO  
N OF REPORT  
Unclassified

18. SECURITY CLASSIFICATION OF  
THIS PAGE  
Unclassified

19. SECURITY CLASSIFI- CATION  
OF ABSTRACT  
Unclassified

20. LIMITATION OF  
ABSTRACT  
UL



Approved for public release; distribution is unlimited

**EVOLUTION OF BEDFORMS ON THE INNER-SHELF**

Damon Beecher Dixon  
Lieutenant, United States Navy  
B.S., United States Naval Academy, Annapolis Maryland, 1995

Submitted in partial fulfillment of the  
requirements for the degree of

**MASTER OF SCIENCE IN METEOROLOGY AND PHYSICAL  
OCEANOGRAPHY**

from the

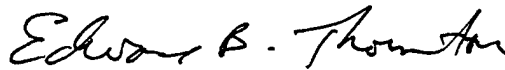
**NAVAL POSTGRADUATE SCHOOL  
September 2000**

Author:



Damon Beecher Dixon

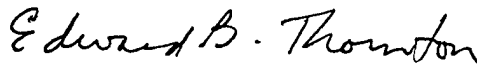
Approved by:



Edward B. Thornton, Thesis Co-Advisor



Timothy P. Stanton, Thesis Co-Advisor



Roland W. Garwood, Chairman  
Department of Oceanography



## ABSTRACT

Observations of the temporal evolution of the wave-formed ripples are analyzed in terms of geometric properties, migration rate, and forcing by wave and current velocities. Three weeks of bedform observations were obtained using underwater video of a sheet of laser light projected on the bed at the Monterey Bay Inner Shelf Observatory in thirteen-meter depth water. The bed consists of fine sand (mean grain size 0.12mm). Low to moderate narrow-band swell waves occurred during the observation period. Ripple geometry consisted of orbital and suborbital vortex wave ripples, and relic ripples left after larger wave events. The bedforms generally changed size and shape when the grain roughness Shields parameter exceeded a critical value of 0.04 with the exception of the last event bringing into question the appropriate value of  $\theta_{crit}$  in nature. Ripple migration was offshore at rates of 2-10 cm/day during active sediment transport events. Skewness of velocities (low and high passed) were calculated to explain offshore ripple migration, but showed no preferred direction. Mean currents were weak and also showed no preferred direction. Significant positive (offshore) correlation was obtained between the short-wave envelope and infragravity waves indicating wave-group forced bound long waves (surf beat) combined with stirring by the short waves might explain the offshore sediment transport and ripple migration.



## TABLE OF CONTENTS

I. INTRODUCTION .....	1
II. EXPERIMENT.....	5
III. RESULTS .....	11
IV. ANALYSIS.....	17
V. CONCLUSION .....	23
LIST OF REFERENCES.....	45
INITIAL DISTRIBUTION LIST.....	47





## LIST OF FIGURES

1. Instrument frame (viewed from sea to shore) at MISO array. ADCP was used to measure current velocities. The PARO was used to calculate wave height and water depth. The camera and structured light provided high resolution video images of bedforms.....25
2. Location of MISO instrument array (a). The star represents the location of the MISO array. Figure 2b. Regional map of central coast of California (b) showing that the Point Pinos headland protects the MISO location and causes waves to be narrow-banded in frequency and direction owing to strong refraction.....26
3. Sand sediment distribution.....27
4. Calibration Coefficient of angle vs distance (a) Horizontal and (b) Vertical. The slope of the line is the calibration coefficient.....28
5. Camera Calibration to convert image from pixel space to real space. Alpha and Beta are angles in the vertical (z) and cross-shore (y) directions.....29
6. Raw image taken from video camera (a). Conversion of video image in pixel space to raw image in real space (cm) (b). Image was rotated because the instrument frame was tilted 12 degrees offshore (c). The image was then smoothed by applying a low pass filter with a 3cm scale (d). The filter did not affect the image resolution which was 1.7mm/pixel.....30
7. Significant Wave Height ( $H_s$ ) for yearday 243-267 of 30-minute averages (a). Rms orbital velocity at the bed ( $u_{brms}$ ) of 30-minute averages (b). Mean currents (cross-shore and alongshore of 1-hour averages) (c).....31
8. Time series of Relative ripple height displayed in greyscale (white is large, dark is small) vs cross-shore distance (positive values are offshore) and time (a). Ripple Crest #1 is the lower ripple crest and Ripple Crest #2 is the upper ripple crest (b). Greatest migration rates occur between 244-248. Grain roughness Shields parameter calculated from a rms orbital velocity averaged every 30 minutes.....32
9. Time evolution of ripple geometries displayed in 3-4 day periods of relative ripple height (greyscale) vs. cross-shore distance (positive is offshore).....33
10. Raw image (a) of long crested ripples on yearday 253 (9/10/99) evolve into shorter bifurcated ripples (b) on yearday 261 (9/18/99). The long crested two are left after the

- strong forcing on yearday 249-252. These give way after the high waves on yearday 259-261 to a short crested bifurcation.....34
11. With maximum slope on the ripple profile is equal to  $\tan \phi$ , the height to length ratio must for geometric reasons be  $0.5 \tan \phi$  for a triangle ripple and  $0.25 \tan \phi$  for a parabolic ripple (after Nielsen 1992.....35
12. Time series of ripple steepness/ $\tan \phi$ . Bed slope geometry data generally falls between  $0.25 < \frac{\eta/\lambda}{\tan \phi} < 0.5$ .  $\frac{\eta/\lambda}{\tan \phi} < 0.25$  when  $\theta_{crit}$  is not exceeded.....36
13. Ripple steepness is highly variable (a). Relative ripple length parameterized by orbital excursion (plotted only when  $\theta > \theta_{crit}$ ) decreases as forcing and orbital excursion increases (b). The dashed line corresponds to  $\lambda \cong 1.3A$  .....37
14. Ripple Geometry (Clifton and Dingler, 1976) classified into orbital, ( $2A/d_{50}$ )  $< 2000$ , suborbital,  $2000 < 2A/d_{50} < 5000$ , and, anorbital,  $2A/d_{50} > 5000$  (a). Time series of  $\lambda$  and  $A$ . Only values of  $A$  have been plotted when  $\theta > \theta_{crit}$  (b).....38
15. Left panel show evolution of selected images of cross-shore distance (positive is offshore) vs relative ripple height. Right panel shows histogram of slope angle with mean slope angle displayed above histogram. Mean slope angles were calculated by averaging the slope angle between crest and succeeding trough. The negative slopes angle are the mean slopes on the off shore side, while the positive slope angle are the slope angles on the onshore side.....39
16. Ripple Asymmetry (a): Large positive values show steeper sloping ripples on the off-shore side while small values show symmetric ripples. Negative values show steeper sloping ripples on the on-shore side. Asymmetric ripples were left after strong wave forcing (high value of Shields Parameter) (b) and tended toward symmetry as the forcing subsided.....40
17. Skewness of cross-shore orbital velocity from surface gravity waves. A high pass filter at 0.05 Hz was applied to the cross-shore velocity time series and skewness values were calculated over one-hour samples.....41
18. Change in momentum (high waves) is balanced by set down of forced long wave and small waves are balanced by a relative set-up. The forced long wave gives reverse

flow under high wave and forward flow under small waves. Because more sediment is suspended during the larger waves. Net transport is reversed or offshore.....42

19. Correlation Coefficient (a) determined by correlating the infragravity wave band (obtained by low pass filtering the cross-shore velocity at 0.05 Hz) with the envelope of the sea-swell band of frequencies. The dashed lines represent the significant correlation. Correlation as calculated in (a), but is not normalized (b). Correlation is determined by  $u_{lp} * (u_{lp})^2$  ..... 43

## ACKNOWLEDGEMENT

Distinguished Professor Ed Thornton and Prof. Tim Stanton, my advisors, generously provided outstanding professional guidance and instruction throughout the entire research process. I thank them for exceptional professional advice, patience, and support - all of which were essential in the completion of this study.

This study would have not been accomplished without the technical expertise of several individuals including, Mark Orzech, Jim Stockel, Rob Wyland, Ad Reniers, Bruce Morris, and Edith Gallager. I am thankful for their support and assistance with the numerous technical issues surrounding the accomplishment of this study.

Research was funded by Office of Naval Research, Coastal Sciences Program, under contract N00114-95-AF-002.

Above all, I would like to thank my family. The patience, flexibility, and encouragement of my wife Cydney, who was a wonderful comfort. Without her love and support, I could not have finished. Also, I would like to thank my parents for teaching me the importance of a well-rounded education. Thanks to all!

## I. INTRODUCTION

As shoaling waves move from deep to shallow water over a sandy bottom, energy dissipation increases in the bottom boundary layer because of the presence of bed roughness in the form of wave-induced ripples. Ripple bedforms in coastal shallow water play a significant role in the interaction of bottom boundary hydrodynamics and sediment transport. When wave energy is sufficient, frictional stresses at the bottom cause wave-induced ripples to form. The flow over the ripples is dominated by the vortices created at the crest on the lee side of the ripples, which also act to enhance wave dissipation. Sediment transport is then dominated by avalanches of sand rolling down on the sides of the ripples, which is much larger than for a flat bed (Andersen 1999). Wave ripples, termed vortex ripples by Bagnold (1946), are triangular in shape with the slope of the sides being close to the angle of repose, usually shorter than 60 cm and not higher than about 6 cm (Engelund and Fredsoe, 1982). Ripples have complex geometry with different equilibrium shapes and sizes.

Until recently, there have been few observations of bedform generated by waves and currents. Some of the first measurements of bedform generation due to waves and currents over a sandy bottom were by Inman and Bowen (1963). Tanaka and Shuto (1984) performed laboratory experiments on bottom bedforms due to waves and currents interacting both in the cross-shore and along-shore directions, and were the first to provide an empirical formula for the prediction of ripple geometry due to waves and current forcing.

Most ripple wavelengths fall into three categories of wavelengths (Clifton and Dingler, 1984). Orbital scale ripples, or "vortex" ripples, have wavelengths ( $\lambda$ ) that scale with wave orbital diameter ( $2A$ ). Anorbital ripples have wavelengths that depend on sediment grain size ( $d$ ) alone. Suborbital ripples represent a transitional stage between orbital and anorbital ripples and depend on both wave orbital diameter and grain size. Important geometric properties to characterize ripples are their height ( $\eta$ ), steepness (ratio of ripple height to wavelength,  $\eta/\lambda$ ), and cross and along shore symmetry. Symmetry in both these directions is an important property affecting formation and migration rates. A common problem with laboratory data is that the wave periods are generally short due to experimental apparatus limitations. Field studies have the limitations that the relationship between wave forcing and ripple geometry can be complicated due to the range of wave heights, periods, directions, and presence of low frequency currents.

Field experiments have been conducted using a variety of techniques to measure bedforms. Manual observations have been made by divers, which greatly limits the sample area and sample rate. Boyd et al. (1988) and Amos et al. (1988) used photographic measurements to investigate the role of waves and currents in generating bedforms. Rotary sidescan sonar was used by Hay and Wilson (1994) and Traykovski et al. (1999) to measure the horizontal pattern of bedform evolution. Crawford and Hay (1998) developed an underwater video system consisting of a diode laser and a video camera to obtain two-dimensional structures of suspended sediment and bedforms. We have adapted a similar approach to analyzing ripple geometry and bedform evolution.

Measurements described here include waves, ripple formation, and increased wave attenuation. This study is a component of the ONR-sponsored shoaling waves experiment (SHOWEX) with the overall objective of measuring wave transformation mechanisms across the shelf. An underwater video camera in conjunction with a structured light source was used to obtain image sequences of the bottom, providing high-resolution digital pictures of ripples on the sandy bottom. The ability to resolve 1 mm-scale features in the bedforms gives this video imaging system the advantage over previous field experiments. The camera and light source were deployed in 13 meter depth at the Monterey Inner Shelf Observatory (Stanton 1999).

Hypotheses for bed migration mechanisms on the inner-shelf (outside the surfzone) include wave skewness, mean currents combined with wave stirring, and bound long waves. The non-linearity of shoaling waves causes waves to have an onshore skewness owing to more peaked crests and flatter troughs. This results in stronger onshore velocity and weaker offshore velocity with a net onshore sediment transport.

Mean currents act to advect sediments that are stirred up and suspended by wave action. The direction of transport is in the direction of the current, which could be onshore, offshore, or alongshore.

Bound long waves act to transport sediments offshore. Natural waves are not regular, but have a variation in the wave height. A narrow-banded wave train consists of wave groups and associated bound long wave (Longuet-Higgins and Stewart 1964). Shi and Larsen (1984) recognized that bound long waves under wave groups could give an opposing contribution to the transport, because the bound long wave troughs occur under high waves with maximum offshore velocity coinciding with high sediment



concentrations stirred by the wave group, while the onshore motion occurs under the low waves. Deigaard, Jakobsen, and Fredsoe (1999) found the nonlinearity of the turbulent boundary layer and the coupling between the offshore motion and high waves give an offshore mean bed shear stress. From their studies they concluded that bound long waves give an offshore contribution to sediment transport.

The objective of this paper is to analyze observations of bedforms in relation to wave and current forcing. The paper is organized into five sections. The second section describes the experiment and the equipment that was deployed during September 2 to September 24, 1999, calibration and processing data that was acquired. The third section describes the results of ripple geometry and ripple migration analyses. A discussion of the results is included in the fourth section. The conclusion and recommendations finalize this thesis.

## II. EXPERIMENT

The MISO instrument frame consists of a five-meter horizontal beam supported one meter above the bed by two vertical pipes jetted into the bed as displayed in Figure 1. Mounted on the frame is a Broadband Acoustic Doppler Current Profiler (BADCP), under-water video camera, para-scientific pressure sensor, scanning acoustic altimeter, Bistatic Coherent Doppler Velocity and Sediment Profiler (BCDVSP) and structured laser light. MISO is a component of the Rapid Environmental Assessment Laboratory (REAL) and was established July 26, 1999 and continues to be operational. MISO is located 400 meters off Del Monte Beach adjacent to the Naval Postgraduate School Oceanography laboratory. A local map depicting the location of MISO is shown in Figure 2a, and a regional map of California's central coast is shown in Figure 2b. Waves incident to the MISO location in the Southern Monterey Bay tend to be narrow-banded in frequency and direction owing to the strong refraction as they pass over the Monterey Bay Submarine canyon, and protection by Point Pinos headland. The MISO array is located on a sand lens consisting of fine sand with shale outcrops 50 meters on either side. The sand at the MISO site was well-sorted quartz with a 0.125 mm median grain diameter ( $d_{50}$ ) (Figure 3).

The data analyzed here is for a 22-day period from September 2, to September 24, 1999. This period provided comprehensive data from the underwater video camera, BADCP, and para-scientific pressure sensor. The mean water depth was 12.8 m varying from 11.7 m to 13.8 m due to diurnal and semi-diurnal tidal forcing. No significant

storms occurred during this time period. The significant wave height peaked at 1.1 m and averaged 0.5 m.

#### A. BROAD BAND ACOUSTIC DOPPLER CURRENT PROFILER (BADCP)

Three-component velocity profiles with 1-m range resolution were measured using the BADCP. The instrument was situated approximately 1 meter off the seafloor with the center of the first range bin located 2.1 meters from the transducer face. The data were sampled at 0.976 Hz. Spectra were computed using thirty-minute ensembles. The spectra were averaged into fifty logarithmic-spaced frequency bins from 0.01 Hz to 0.35 Hz. Mean-square wave bed velocities were calculated using a linear theory transfer function  $H_b(f)$  to transform measured velocity at 4.1 m,  $S_u(f)$ , to the bed over a 0.05 to 0.3 Hz frequency band

$$U_b^2 = \int_{0.05}^{0.3} [H_b(f)]^2 S_u(f) df \quad (1)$$

where  $H_b(f) = 1/\cosh(k(h+z))$ ,  $k$  is the wavenumber and  $h+z$  is distance above the bed. The rms orbital excursion at the bed ( $A_{brms}$ ) was computed from the band passed velocity spectrum at the bed using the integrating operator,  $H_A(f) = 1/\omega$ , on the frequency spectrum

$$A_{brms} = \sqrt{\int_{0.05}^{0.3} [H_A(f)]^2 S_u(f) df} \quad (2)$$

To determine the importance of mean currents on ripple formation, thirty-second cross-shore and alongshore mean currents were calculated from the BADCP data. It is

hypothesized that semi-diurnal and diurnal tides, winds and baroclinic tidal effects played a role in the forcing of these currents.

## B. PARO-SCIENTIFIC PRESSURE SENSOR

A high precision Paro-Scientific pressure sensor was used to estimate surface elevation and to determine the mean depth of water. Surface elevation spectra were calculated by applying a linear wave transfer function to the pressure spectra,

$$S_{\zeta} = [H_p(f)]^2 S_p(f), \text{ where } H_p(f) = \frac{\cosh(kh)}{\cosh(k(h+z))}. \text{ The depth of water was}$$

calculated from the pressure data averaged every five minutes. The data were acquired at 2 Hz and with a thirty-minute ensemble. Fifty logarithmically-space frequency bins were calculated from 0.001 Hz to 0.2 Hz. Significant wave height was calculated from the surface elevation spectrum

$$H_s = 4 \sqrt{\int_{.05}^{0.3} S_{\zeta}(f) df} \quad (3)$$

## C. VIDEO CAMERA AND LASER LIGHT

Underwater video cameras and structured light sources provide a means to observe sediment movement in near shore environments under conditions of good visibility. The video/laser system consists of two diode lasers and an imaging camera. The diode laser operates in the visible red at 685 nm wavelength with a power of 35 mW. The two lasers are housed in a rectangular pressure case 4.6 inches wide by 6 inches long. A cylindrical lens in front of each laser spreads the point sources into a 60° beam width, 4 mm wide sheet of light. One laser sheet of light is directed in the cross-shore direction,

while the second is directed  $45^\circ$  to the cross-shore direction. The plane of light intersects the bed producing a bright stripe in the video image (see Figure 6a).

A Cohu 4910, RS 170 monochrome camera is connected to one channel of the eight-node power and data controller at the MISO site, which provides serial data communication and a video bandwidth channel to shore. This underwater multi-node controller provides power to each node and converts the electrical video signal into a fiber optic signal for transmission 600 meters to the Marine Operations Building (MOB) on the shore. The electrical video signal is converted to a fiber optic signal to transmit the long distance while retaining low noise and high bandwidth. At MOB, the signal is converted back to a RS 170 signal and digitized by a Haupage frame grabbing board in a Pentium III PC running the Linux operating system. The video frames are sampled at 10 Hz. Each pixel in the images is processed to determine a mean, max, min, standard deviation and raw image stored over each five-minute ensemble. Initially the pixel size is 640 by 480, but is reduced to 320 by 240 in order to conserve storage space and reduce noise.

#### **D. CALIBRATION**

The first step to extract meaningful position data from video images is to calibrate the field of view. To calibrate for underwater lens distortion, the camera was suspended in a laboratory water tank and exact measurements of distance from camera to a test grid were taken. To determine angle versus distance, calibration coefficients were computed in the cross-shore axis [ $\text{cal}(x)$ ] and the ripple height axis [ $\text{cal}(z)$ ] as shown in Figure 4. The calibrations from pixel space to angle for horizontal angle ( $\beta$ ) and vertical angle ( $\alpha$ ) is approximately given by

$$\beta = [pix(x) - 160] * cal(x) \text{ and } \alpha = [pix(z) - 120] * cal(z).$$

The center pixel in each image was located at  $x=160$  and  $z=120$  for the 320 by 240 pixel sized image. Following the geometry in Figure 5, distance from the camera to the bottom is determined by  $z = d * \tan(off + \alpha)$ , where  $d$  is the horizontal distance from the structured light to the focal point of the camera and  $off$  is the angle between the center pixel of the camera and the horizontal frame. For the data considered here,  $off$  is equal to 47.48 degrees and  $d = 111.76$  cm. The cross-shore distance is estimated by

$$x = \frac{d}{\cos(off)} * \tan(\beta).$$

Since the instrument frame was tilted 12 degrees in the offshore direction during these observations, the raw image had to be rotated. Once rotated, the image was smoothed by filtering the data using a fourth order low-pass filter with a 2 cm cut off to produce a clean line representing relative ripple height in the cross-shore direction, with positive values of the cross-section signifying the offshore direction as displayed in Figure 6. The low-pass filter had negligible effect on measured slopes.

During strong wave forcing, turbid conditions existed and video image resolution was significantly impaired. However, most of the time visibility was high, and the camera provided a high-resolution, two-dimensional time series of the cross-shore bed height over a 54 cm cross-shore distance with 1.7 mm/pixel resolution.

THIS PAGE INTENTIONALLY LEFT BLANK

### III. RESULTS

Wave induced ripple formation is related to the ability of waves to move sediment, which can be described by the Shields parameter. The Shields parameter is the ratio of the force mobilizing the sediments, measured by the bottom stress ( $\tau_b$ ), to the restoring force of gravity

$$\theta = \tau_b / (s-1)gd_{50} \quad (4)$$

where  $s$  is the ratio of sediment grain density to water density and is equal to 2.65 for quartz sand,  $g$  is the force of gravity, and  $d_{50}$  is the mean grain size. Bottom stress can be divided into form drag and skin friction, where skin friction is primarily responsible for sediment motion and includes the effects of both waves and currents. Assuming a classic square law friction factor, and partitioning the stress into wave and current contributions, the equation for bed stress is:

$$\tau_b = \tau_w + \tau_c = \frac{1}{2}\rho f_w \langle u_w^2 \rangle + \frac{1}{2}\rho f_c \langle U_m^2 + V_m^2 \rangle \quad (5)$$

where  $u_w$  is the rms wave velocity at the bed,  $U, V$  are the cross-shore and alongshore mean current velocities, and  $\rho$  is water density. The wave friction factor,

$f_w = \exp[5.213(\frac{2.5d_{50}}{A})^{0.194} - 5.977]$  is based on Swart's (1974) formula using the value

$2.5d_{50}$  for the grain roughness of a flat bed (Fredsoe and Deigaard, 1992), where  $A$  is the orbital excursion radius. The current friction factor is  $f_c = .003$  (Amos et al., 1988). The initiation of sediment movement occurs when the grain roughness shields parameter



is greater than the critical shields parameter  $\theta_{crit} = .04$  (Grant and Madsen 1976), which is consistent with combined mean and oscillatory flows (Amos et al., 1988).

The evolution of ripple patterns is displayed by examining sequences of the 5-minute mean images. Computer animated movies of the mean images provide a detailed view of these processes (<http://www.oc.nps.navy.mil/~stanton/miso/dixon>). The 22-day period of observation from yearday 245 through yearday 267 coincided with two wave events, two to three days in duration (Figure 7a). A wave event also preceded yearday 245, which is included in the wave climatology. The wave-induced cross-shore bed velocity (Figure 7b) reflects the changes in wave height. The mean currents (Figure 7c) were weak with alongshore currents (<0.1m/s) stronger than the cross-shore currents (<0.05m/s). Diurnal variation in these currents (either due to tide or diurnal sea breeze) is evident. The combination of larger wave events succeeded by relatively small wave events created highly variable bedform evolution.

Ripple wavelengths and migration are summarized in Figure 8a, which shows ripple height (grayscale intensity) versus cross-shore distance and time. The dotted lines are the crests of two ripples determined by a change in slope from positive to negative. Migration rates are determined from the slope of the crest line. The table describes ripple crest migration rates.

Yearday	246-248	248.5-249.4	254-257	259.5-262	264-265.3
Crest#1(cm/day)	6.84	-5.6	1.22	6.3	5.04
Crest#2(cm/day)	10.35	-6.23/7.07	1.89		

Significant migration occurs between 246-248, 248.5-249.4 and 259.5-262. On yearday 248.5, a bifurcation occurs as crest #2 separates, leaving one crest that continues to migrate offshore, while a second crest migrates onshore. On yearday 265, it is interesting to note that while forcing is low ( $\theta < \theta_{crit}$ ), crest #1 migrates offshore fairly swiftly but crest #2 does not move. It is not understood what causes these differences in migration directions, however it is hypothesized that the crests are associated with a more three dimensional bedform.

The Shields parameter was calculated using the measured BADCP velocities partitioned into wave mean square velocities (Equation 1) and mean current velocities. The wave velocities were approximately an order of magnitude greater than the mean current velocities. In addition, the wave friction factor is an order magnitude greater than the current friction factor. Hence, the contribution to the Shields parameter by the mean current was negligible (2 percent on average).

Marginally active ripple patterns and evolution were seen throughout the period of observation despite the fact that the grain roughness Shields parameter (Equation 4) often dips below the critical Shields parameter  $\theta_{crit} = .04$  (Figure 8b). The video imaging system did not produce bedform images during daylight hours because the solar illumination usually swamped the structured laser light sheet. Therefore, each day is missing approximately 7 hours of images. Images are also missing during a large wave event between yeardays 249.5 and 252, because turbidity is strong during high sediment suspension.

Ripple length  $\lambda$ , is the distance from crest to crest and ripple height,  $\eta$ , is the difference between the elevations of the crest and succeeding trough. A maximum angle

( $\phi$ ) of the ripple is calculated as the maximum angle occurring between a crest and succeeding trough, while the slope angle is the average angle between the crest and succeeding trough,  $\eta/\lambda$ . Maximum angle ( $\phi$ ) was determined by computing the difference in  $\tan^{-1}(\Delta\eta/\Delta x)$  with  $\Delta x = 0.8$  cm being the image resolution. The slope angles were found not to be sensitive to the choice of  $\Delta x$  values, which was varied between 0.8 and 2.4 cm.

Images of the evolving ripple geometries are shown in Figure 9, where 3-4 day time series of data are plotted against relative ripple height and cross-shore distance. Observations begin with relic ripples during yearday 245, which are left over from the large wave days between yeardays 242-244. Relic ripples have smaller slope angles and more rounded crest than active vortex ripples. By yearday 246,  $\theta$  exceeds  $\theta_{crit}$  and wave ripples begin to form. These are pointed, active vortex ripples, which shed vortices regularly. The Shields parameter remains above the  $\theta_{crit}$  threshold between yeardays 246 and 249, during which time ripple migration is weakly offshore; however, due to the lack of bed profiles during these days, the ripple migration is difficult to resolve. The ripples are moderately asymmetric containing a steeper slope on the leeward (off-shore) side. During yearday 249, strong wave forcing caused strong sediment suspension, which blocked the vision of the video camera so that bed profiles were not recovered between yeardays 249.5 and 252. During this two and a half-day period, the Shields parameter reached a maximum over the twenty-two day time period. It cannot be determined if the ripples migrated onshore or offshore during this period of time

On yearday 252, the waves calmed with  $\theta$  below  $\theta_{crit}$  until yearday 254 leaving relic ripples, which significantly increase in size as only two crests dominate over the 57 cm cross section. The ripple length of 30 cm between these successive crests is the longest during the entire period. Between yearday 252-254, the ripples are inactive representing relic ripples. From yearday 254-256,  $\theta$  is above the threshold value and bedforms begin to move slowly, migrating at a rate of 4-5 cm/day. This well organized long crested wave ripple is sustained as the bedform migrates seaward.

Ripple migration ceases on yearday 256.5 as  $\theta$  is below  $\theta_{crit}$  and relic ripples prevail. The long crested wave ripple remains intact until yearday 258.5 when the second largest wave day begins with  $\theta$  well above  $\theta_{crit}$ , and the ripples are active. Vortex ripples occur during the larger wave days, and their geometry is highly variable. Ripple migration begins at the same time that the large swell arrives (yearday 259). Migration rates are equal to that of the previous period at 5 cm/day. The long crested ripples that dominated earlier give way to shorter bifurcated three-dimensional ripples during yeardays 261 –263 (Figures 10a and 10b). Two ripple crests dominated the bed between 252-259. The wave event (yearday 259) stirs the bed producing the bifurcation and three-dimensional ripples that are seen on yearday 261. Between yearday 261 and 265, wave energy is weak, and ripples are less active but continue to migrate a few cm/day. Bed movement slowly decreases and ripple migration comes to a halt on yearday 264. There is a small burst of wave energy on yearday 265, and ripples are highly active. From yeardays 266-267, wave energy is low and bedform variability is limited. The three-

dimensional bifurcated ripple gives way to symmetric gently sloping ripples on yearday 267.

In summary, the observation period is marked by three wave events. The first occurs prior to the start of ripple observation, the second wave event (249-252) is too strong to obtain bedform images, and bedform geometry is highly variable during the third wave event. It is during these larger wave events that ripple migration rates are the highest while ripples are strongly asymmetric with steeper slopes on the leeward side of the crest. Immediately following the larger wave events, relic ripples prevail as  $\theta$  is below  $\theta_{crit}$ . Once wave energy increases slightly, ripples begin to migrate, although their geometry does not significantly change. The migrating vortex ripples yield to relic ripples as wave energy decreases and the pattern starts over.

#### IV. DISCUSSION

Ripple steepness is limited by the angle of repose of the wet sand, where  $\phi$  is the local maximum angle between crest and succeeding trough. Assuming the ripple is a triangle, Nielsen (1981) suggests that the maximum steepness a bedform can obtain

$(\eta/\lambda) = 0.5 \tan \phi$ . If the trough had the shape of a parabola, the limit would be

$(\eta/\lambda) = 0.25 \tan \phi$  as displayed in Figure 11. Most of the bed slope data from the observations lies within the interval  $0.25 \tan \phi < (\eta/\lambda) < 0.5 \tan \phi$  (Figure 12). Nielsen (1979) found that ripples maintain their maximum steepness when  $\theta < 0.2$  but, when  $\theta > 0.2$ , the vortex can no longer maintain the maximum steepness against the erosion of the crest. The result is that  $\eta/\lambda$  decreases as water particle velocity increases, and at stronger forcing ripples disappear completely. During the observation period,  $\theta$  peaked at 0.12 and we do not see  $\eta/\lambda$  decreasing as a function of water particle velocity (Figure 13a). Ripple steepness varied between 0.04 and 0.26 at low values of  $\theta < \theta_{crit}$ , indicative of relic ripples.

The ripple length has been suggested to be related to the orbital diameter ( $2A$ ) of the wave-induced fluid motion near the bed,  $\lambda \cong 1.3A$  (Nielsen 1992). However, we find significant variation of  $\lambda/A$  over the range  $\theta < 0.05$ , with  $\lambda/A$  decreasing to an approximate value of 1.3 (Figure 13b). One has to be careful in the interpretation of the apparent decrease in  $\lambda/A$  with increasing mobility number as  $\theta \propto u^2 = A^2/\omega^2$ .

Therefore, both the ordinate and abscissa contain the same variable. Similar plots have been widely reported in the literature (Nielsen, 1992). For the larger value of  $\theta$ ,  $\lambda/A$  approaches 1.3 independent of  $\theta$  in the range of  $\theta > 0.11$  up to the maximum value of 0.21.

Clifton and Dingler (1984) summarized several data sets from laboratory and field studies and suggested that that ripple wavelength scales linearly with orbital diameter for shorter period waves until orbital diameter/grain size ( $2A/d_{50}$ ) reaches a value of 2000. These are described as orbital or vortex ripples (Bagnold, 1946). In the range of  $2000 < 2A/d_{50} < 5000$ , for longer period waves with increased orbital excursion, the ripples go through a transitional stage, where ripples are much shorter and are referred to as suborbital ripples. For values of  $2A/d_{50} > 5000$ , when orbital diameter is larger, ripple wavelength scales directly with grain size. The bedform environment was in a state of flux during the observation period. Orbital and suborbital ripples were the dominant ripple pattern (Figure 14). However, when wave forcing was small, relic ripples were present. The period starts with remnant or relic ripples, which are left over from the larger waves on yearday 243-244. These appear to be suborbital relic ripples as  $2A/d_{50}$  fell between 2000 and 5000 on yearday 244. Ripples tend to orbital ripples on yearday 246 as ripple length scales approach orbital excursion. The bed is in constant motion with ripple steepness peaking on yearday 246 and the steepness of these vortex ripples approach their angle of repose. When the largest waves of the observation period arrive

on yearday 249.4, no images are retrieved, but it can be hypothesized that these are highly active suborbital ripples. When the waves subsided, suborbital relic ripples were left. The strong wave forcing changed the bedforms to two ripple crest spaced 30 cm apart. When the next large wave event occurs on yearday 259, ripple length scales with orbital excursion and orbital ripples are formed. Once the forcing ceases, orbital relic ripples remain and continue through to the end of the observation period.

Ripples become asymmetric when suspended sediments are lifted and carried from the upstream side trough and settle on downstream side crest. In the following discussion, upstream is the side of the ripple where the sediment is moving from and downstream is the location where the sediment is moving. The building up of the downstream side crest creates a steeper slope on the downstream side and a shallower slope on the upstream side. As this process continues, the downstream side becomes steeper and the upstream side becomes shallower. Active asymmetric ripples migrate in the direction of the steeper slope, while active symmetric ripples may not change their position. For example, during yearday 254, the leeward slope is twice as steep as the windward slope indicative that the ripples are migrating in the offshore direction (see histograms of slope angle for selected ripple profiles in Figure 15).

Mean slope angles were calculated by subtracting the mean slopes of the offshore and onshore sides of the ripple to determine ripple symmetry. Large positive values represent asymmetric ripples with a steeper slope on the offshore side, indicative of ripples migrating offshore (negative slopes indicate onshore migration) while small values correspond to symmetric ripples (Figure 16). Asymmetric ripples were formed following the wave events and slowly eroded with weaker forcing. The forcing by larger



waves on yeardays 243-244 appears to have resulted in the observed asymmetric ripples on yeardays 245-246. These bedforms became symmetric as the wave forcing subsided. The larger waves starting on yearday 248 had large onshore, negative skewness (see Figure 17) coinciding with onshore migration (see Figure 8a) and ripple asymmetry indicative of onshore transport. From yeardays 250-253,  $\theta$  decreased and skewness changed from onshore to offshore. When the images resumed, ripples migrated onshore (yeardays 253-257) and were asymmetric. As wave forcing decreased, migration rates slowed and ripples became symmetric. During the last wave event (yeardays 259-262) migration rates were strong. Ripples became asymmetric for a short time on yearday 263 and tended toward symmetry as the period of observation concluded.

Mean and skewness velocities were calculated to assess if they could explain offshore ripple migration. Skewness of low-passed and high-passed filtered velocities (0.05 Hz cut-off), most of the time showed no preferred direction (Figure 17). The exceptional times when onshore, negative skewness exceeded 0.1 occurred on yeardays 250 and 265 when migration was onshore. Cross-shore mean current were weak and fluctuated between the offshore and onshore direction, again suggesting no preferred direction (see Figure 7c).

Bound long waves give an offshore contribution to sediment transport and can result in offshore ripple migration as schematically shown in Figure 18. The presence of bound long waves was measured by correlating the infragravity wave band (obtained by low passing the cross-shore velocity below 0.05 Hz) with the envelope of the sea-swell band of frequencies (Hanes 1991) as shown in Figure 19a. The envelope of the sea-swell band is obtained by low pass filtering (below 0.05 Hz) the  $u^2$  time series. Positive

correlation suggests bound long waves, (coordinate system is  $u$  positive offshore). The correlations are significantly different than zero at the 95% confidence level (assuming Gaussian velocities) for  $-0.0167 < r < 0.0167$ . The  $r$  values are persistently positive and mostly significant indicating bound long waves were present

A measure of sediment transport advected by bound long waves is given by  $u_{lp} * (u^2)_{lp}$  where sediment transport is parameterized as proportional to  $(u^2)_{lp}$  (Figure 19b). Transport was mostly offshore in agreement with ripple migration direction.

Four offshore ripple migration events occurred between 246-248, 254-257, 259.5-262, and 264-265.3 as shown in Figure 9. The first event yielded the swiftest migration rates. Orbital forcing was strong enough for  $\theta_{crit}$  threshold to be surpassed. Two ripples dominated at the start of yearday 246 and the ripple #2 migrated at 10.35 cm/day while ripple #1 migrated at 6.84 cm/day. During this time frame, waves were groupy and bound long waves were present. The migration rate was low during the second event as  $\theta_{crit}$  was exceeded only during yearday 255 by 0.02. These ripples migrated offshore at 1.5 cm/day. Bound long waves were present and ripples slowly migrated offshore. Yeardays 259.5 and 262 provide good information because although the forcing was strong, video images were obtained. The presence of bound long waves caused the ripples to migrate offshore at 6.3 cm/day.

There is a question of what causes the final event to migrate offshore at 5.0 cm/sec when  $\theta < \theta_{crit}$ . This brings into question the validity of  $\theta_{crit}=0.04$  or how this value is applied. By viewing the video showing ripple forms migrating along with calculated Shields parameter, it is qualitatively observed that the bed only migrated when

$\theta > \theta_{crit}$  with exception of yearday 264. The basis for  $\theta_{crit}=0.04$  are laboratory experiments using monochromatic waves with constant amplitude (Grant and Madsen, 1976). The wave velocity is a bulk rms value for a 30 minute ensemble and does not accurately capture the large range of forcing between the peak and minima within a wave group. For very narrow banded, groupy waves in nature, the maximum wave velocity could be more two-five times the monochromatic value for the same Shields Parameter. Therefore, it is hypothesized  $\theta_{crit}$  may be less than 0.4 for waves in nature.

## V. CONCLUSION

The analysis of bedform evolution using an underwater video camera in conjunction with a laser light has been demonstrated. High-resolution images were obtained and analyzed in relation to wave and current forcing. Ripple geometry and migration rates were obtained. The following conclusions are made.

Ripple steepness varied for values of  $\theta$ , and no relationship was found. Relative ripple length ( $\lambda/A$ ) decreases as a function of the Shields parameter and was approximately constant at 1.3 in the range of  $0.07 < \theta < 0.21$ . Ripples were steeper on the downstream or offshore side. Asymmetric ripples were left after large wave events and tended toward symmetry with weaker forcing. Orbital ripples were the dominant bedform found when the wave and current forcing was strong. However, when the waves relaxed relic ripples prevailed. Forcing was never strong enough such that orbital excursion could reach a value to create anorbital ripples, however, suborbital ripples were formed during the strongest forcing event.

Migration of ripples may be the dominant mode of cross-shore sediment transport at the MISO site. Measured migration rates occurred in four events (246-248, 254-257, 259.5-262, and 264-265.3), and all ripples actively migrated offshore. During these events,  $\theta$  exceeded the critical shields parameter on all days except during yearday 264-265.3. Skewness of orbital velocity (both high and low passed) mostly showed no preferred direction to explain offshore ripple migration. Significant positive correlation was obtained between wave groupiness of the narrow banded swell, (measured as the

envelope of high passed velocity signal), and bound long waves, which may account for the offshore migration during the first three events.

The use of video imaging to accurately map the bedform evolution was successful, however when large waves caused strong sediment mixing, no video images were obtained. Hence ripple information was limited to low wave events.

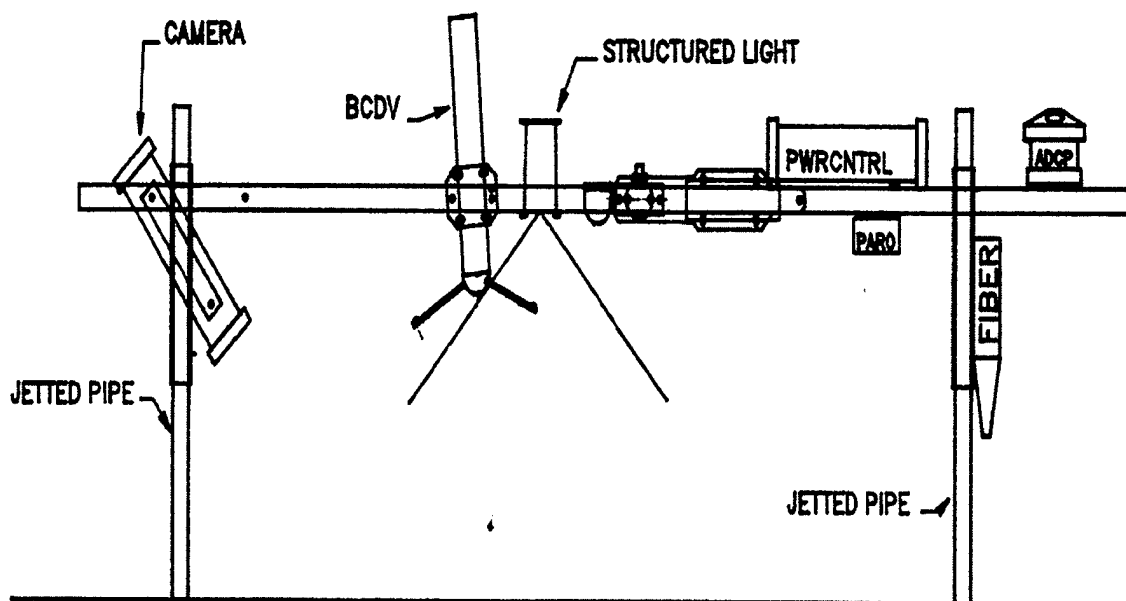


Figure 1. Instrument frame (viewed from sea to shore) at MISO array. ADCP was used to measure current velocities. The PARO was used to calculate wave height and water depth. The camera and structured light provided high resolution video images of bedforms.

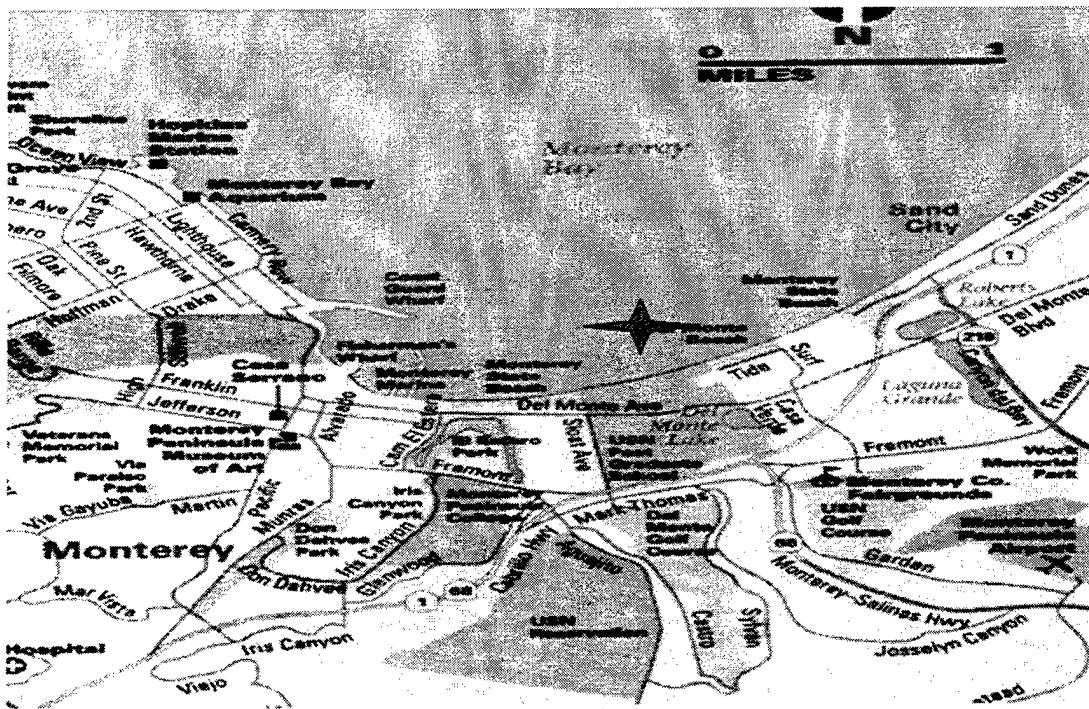


Figure 2a



Figure 2b

Figure 2a. Location of MISO instrument array. The star represents the location of the MISO array. Figure 2b. Regional map of central coast of California showing that the Point Pinos headland protects the MISO location and causes waves to be narrow-banded in frequency and direction owing to strong refraction.

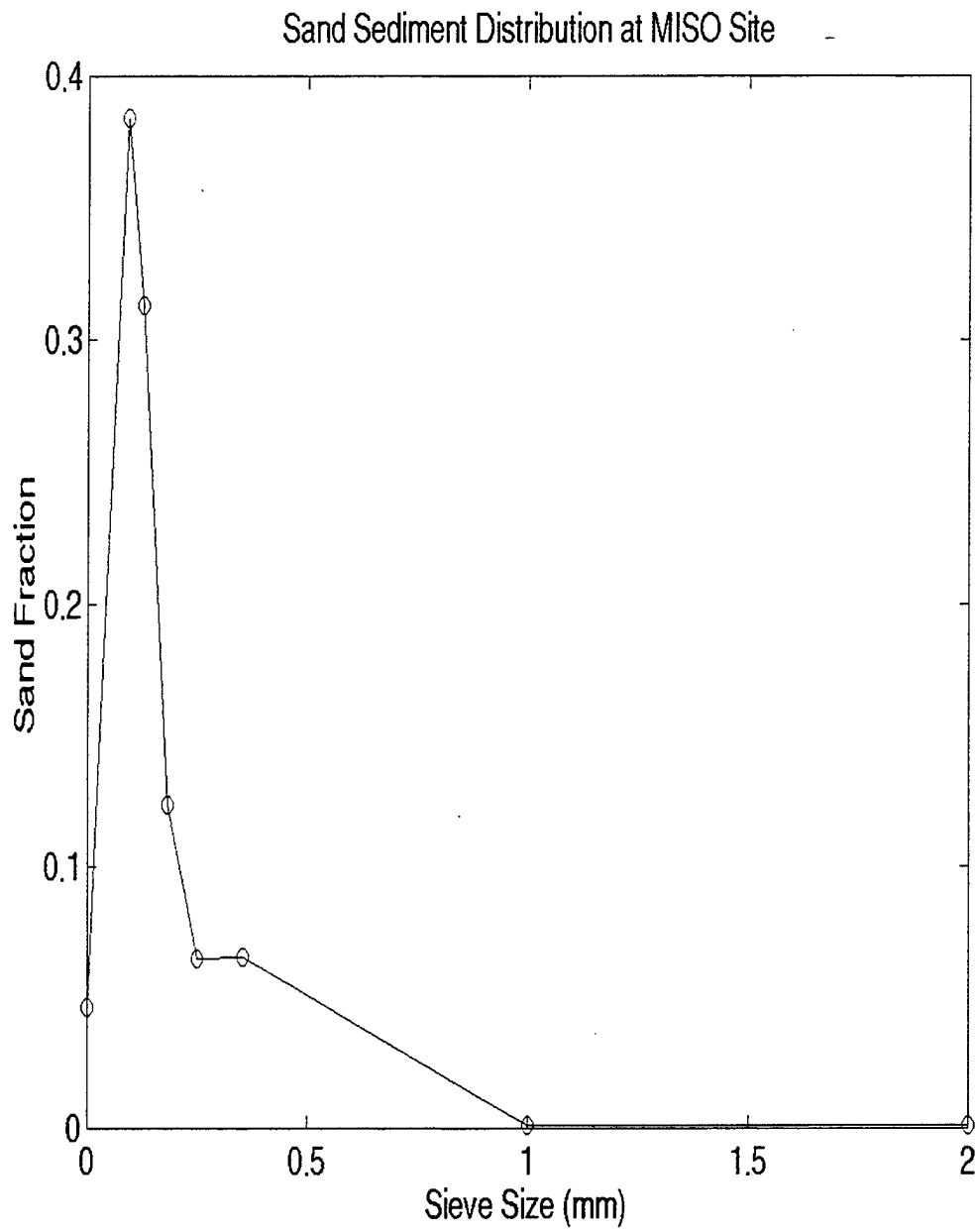


Figure 3. Sand Grain Size Distribution with median grain size ( $d_{50}$ )=0.125 mm



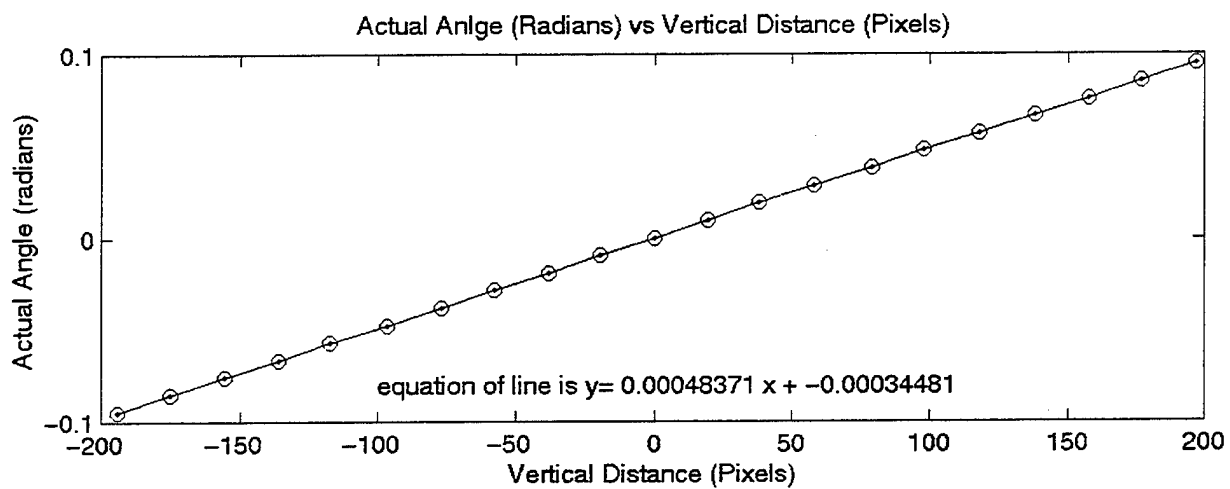
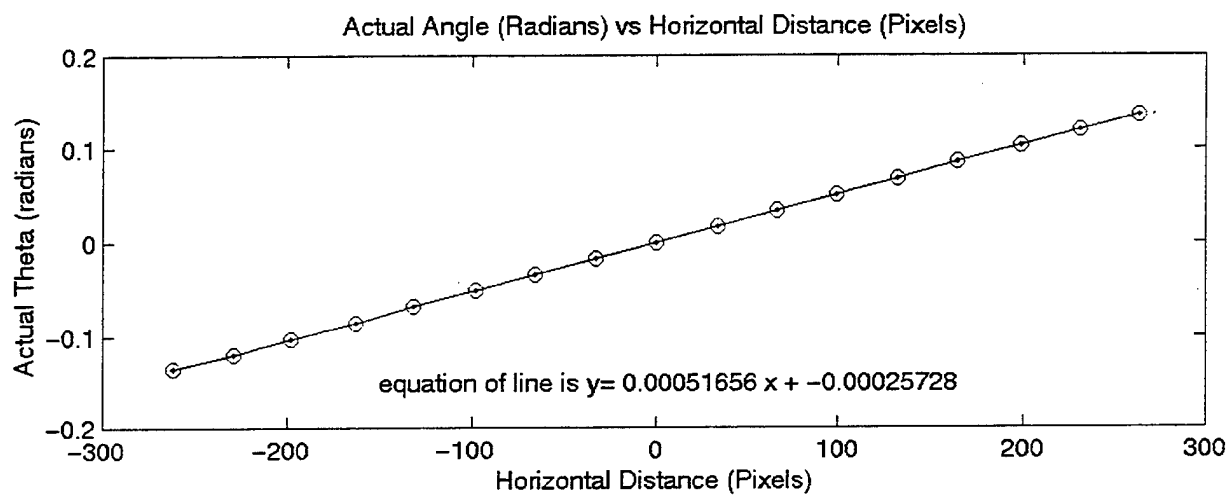


Figure 4a. Horizontal calibration Figure 4b. Vertical calibration. The slope of the line is the calibration coefficient.

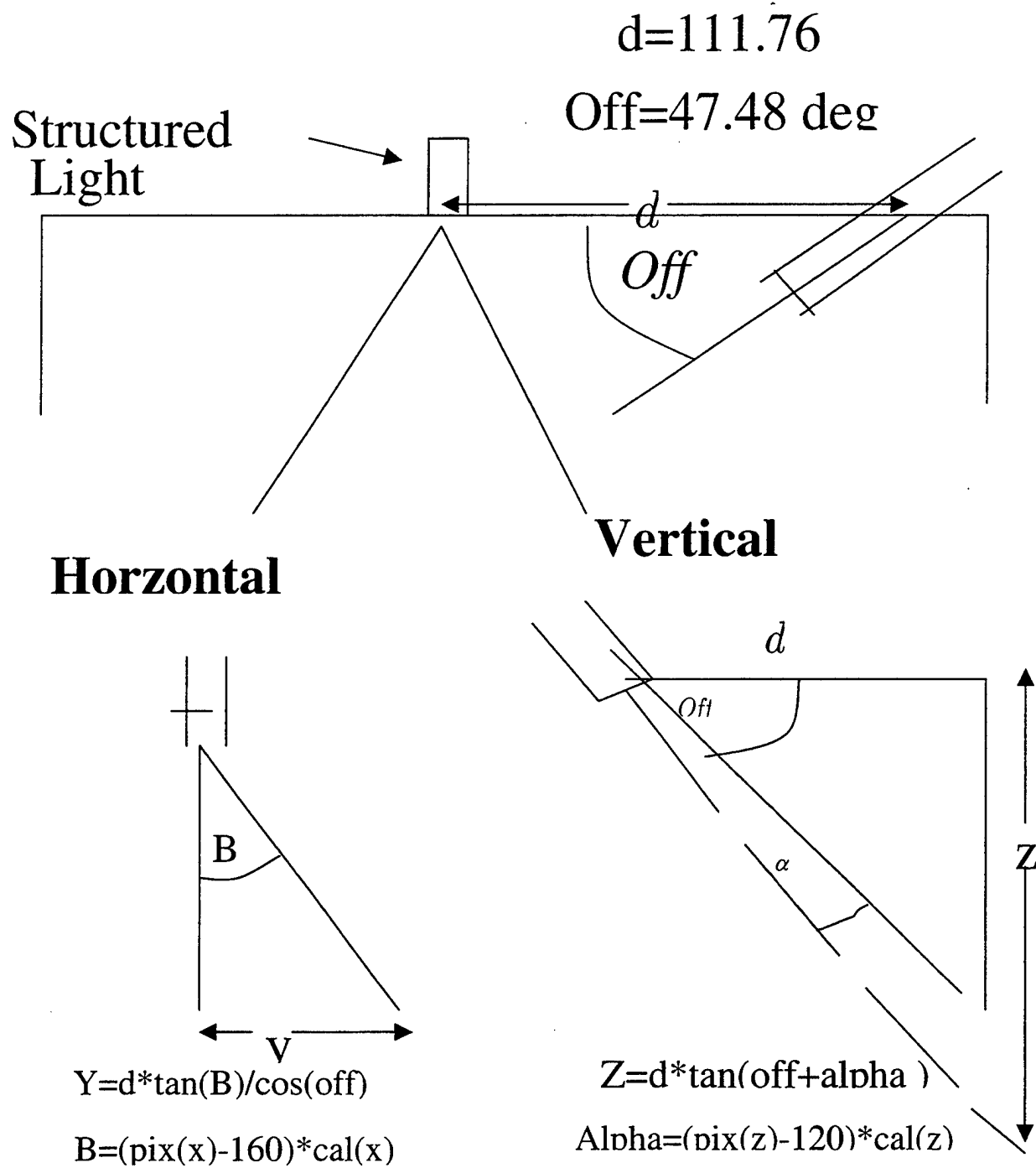


Figure 5. Camera calibration showing horizontal and vertical cross-sections. Alpha and B are angles in the vertical (z) and cross-shore (y) directions.

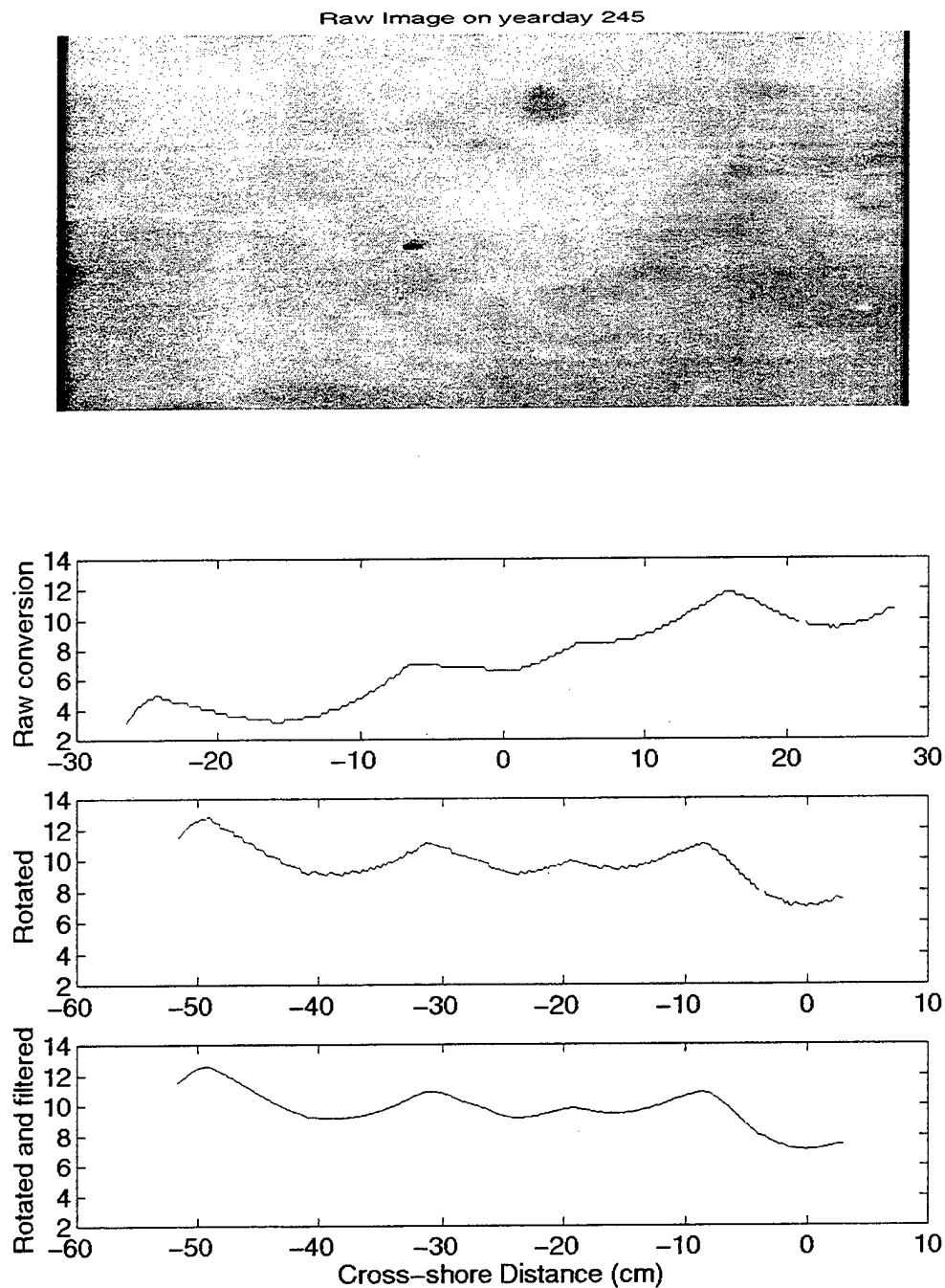


Figure 6a. Raw image taken from video camera. Figure 6b. Conversion of video image in pixel space to raw image in real space (cm). Figure 6c. Image was rotated because the instrument frame was tilted 12 degrees offshore. Figure 6d. The image was then smoothed by applying a low pass filter with a 3cm scale. The filter did not affect the image resolution which was 1.7mm/pixel.

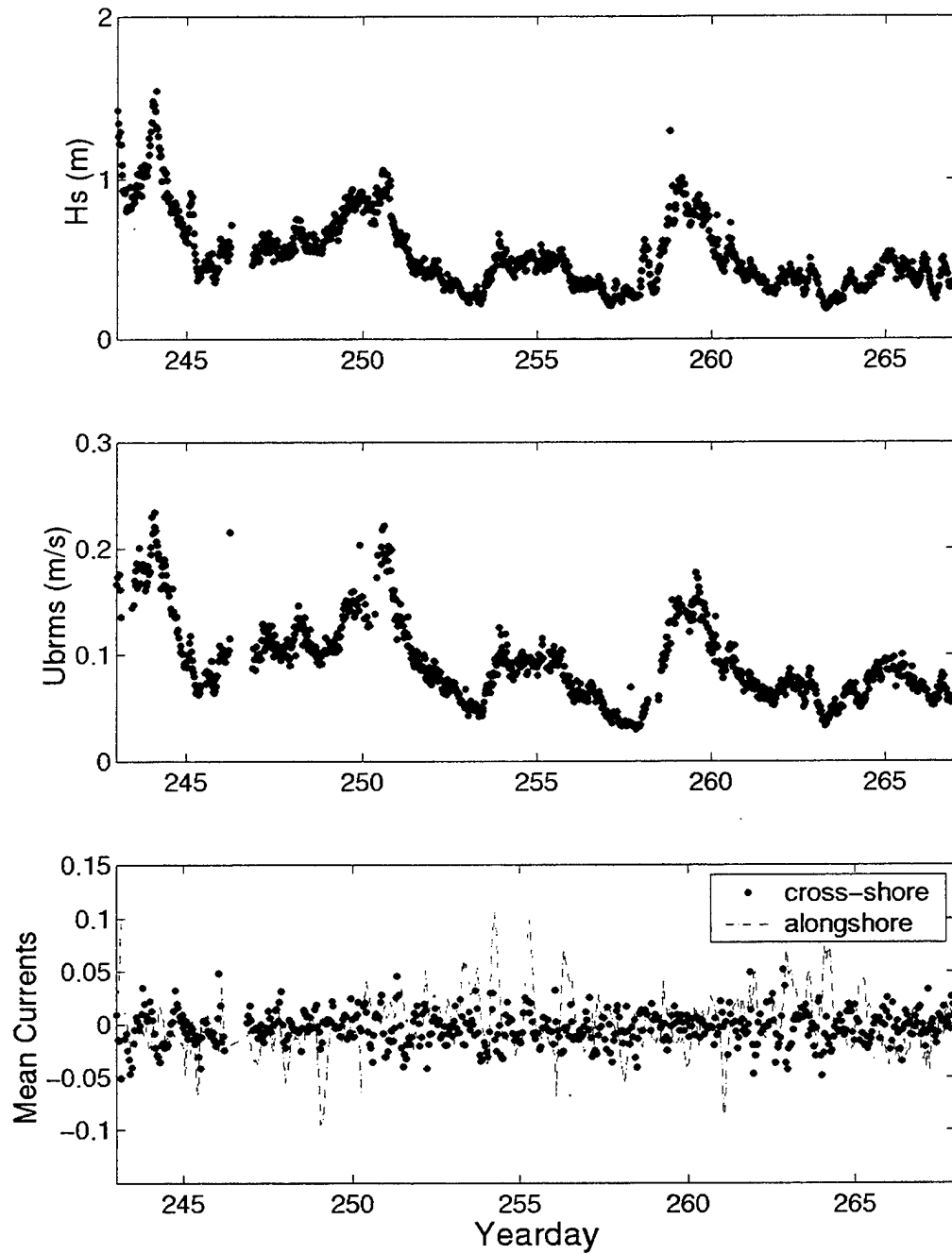


Figure 7a. Significant Wave Height ( $H_s$ ) for yearday 243-267 of 30-minute averages. Figure 7b. Rms orbital velocity at the bed ( $u_{brms}$ ) of 30-minute averages. Figure 7c. Mean currents (cross-shore and alongshore of 1-hour averages).

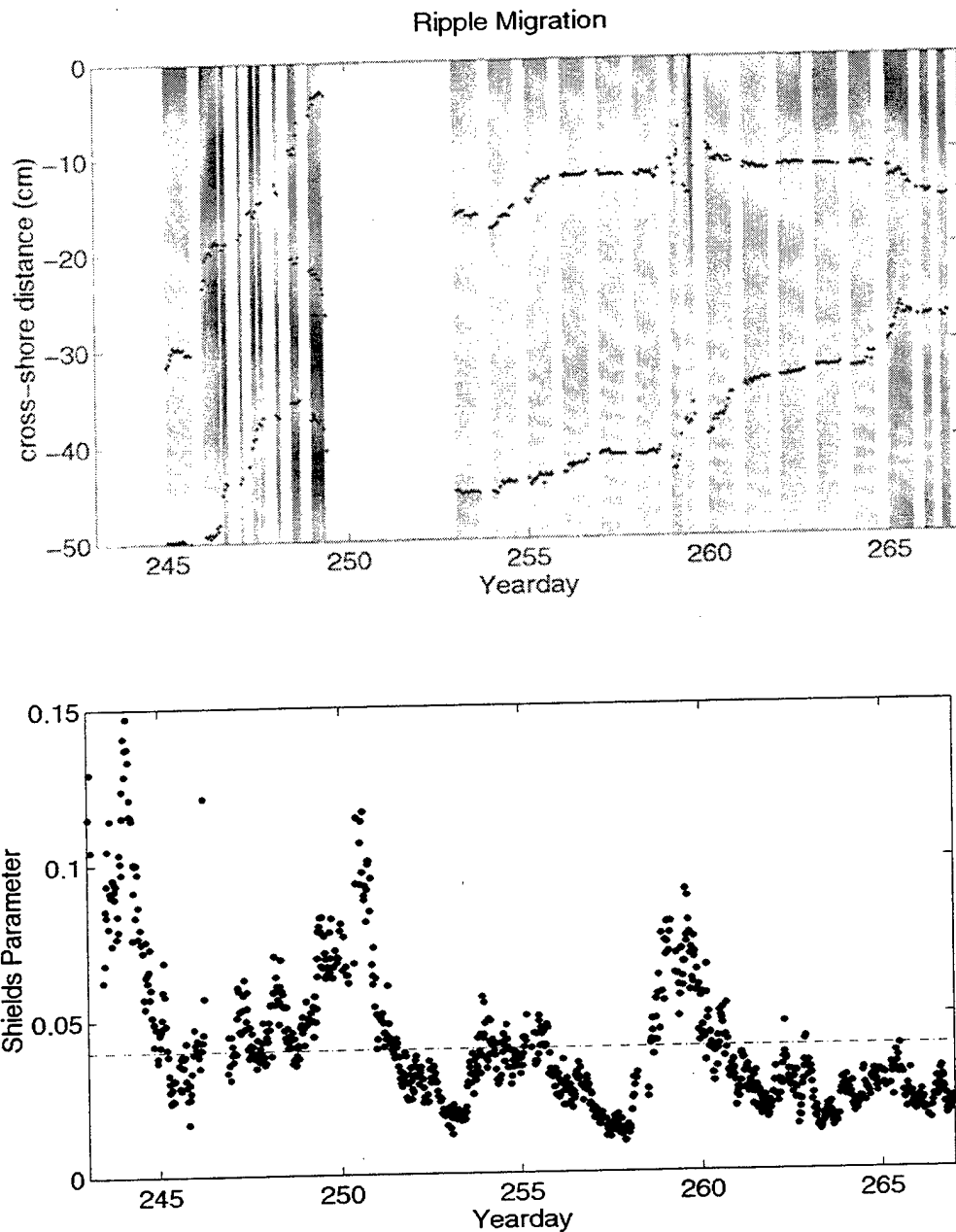


Figure 8a. Time series of Relative ripple height displayed in grayscale (white is large, dark is small) vs. cross-shore distance (positive values are offshore) and time. Ripple Crest #1 is the lower ripple crest and Ripple Crest #2 is the upper ripple crest. Greatest migration rates occur between 244-248. Figure 8b. Grain roughness Shields parameter calculated from a rms orbital velocity averaged every 30 minutes.

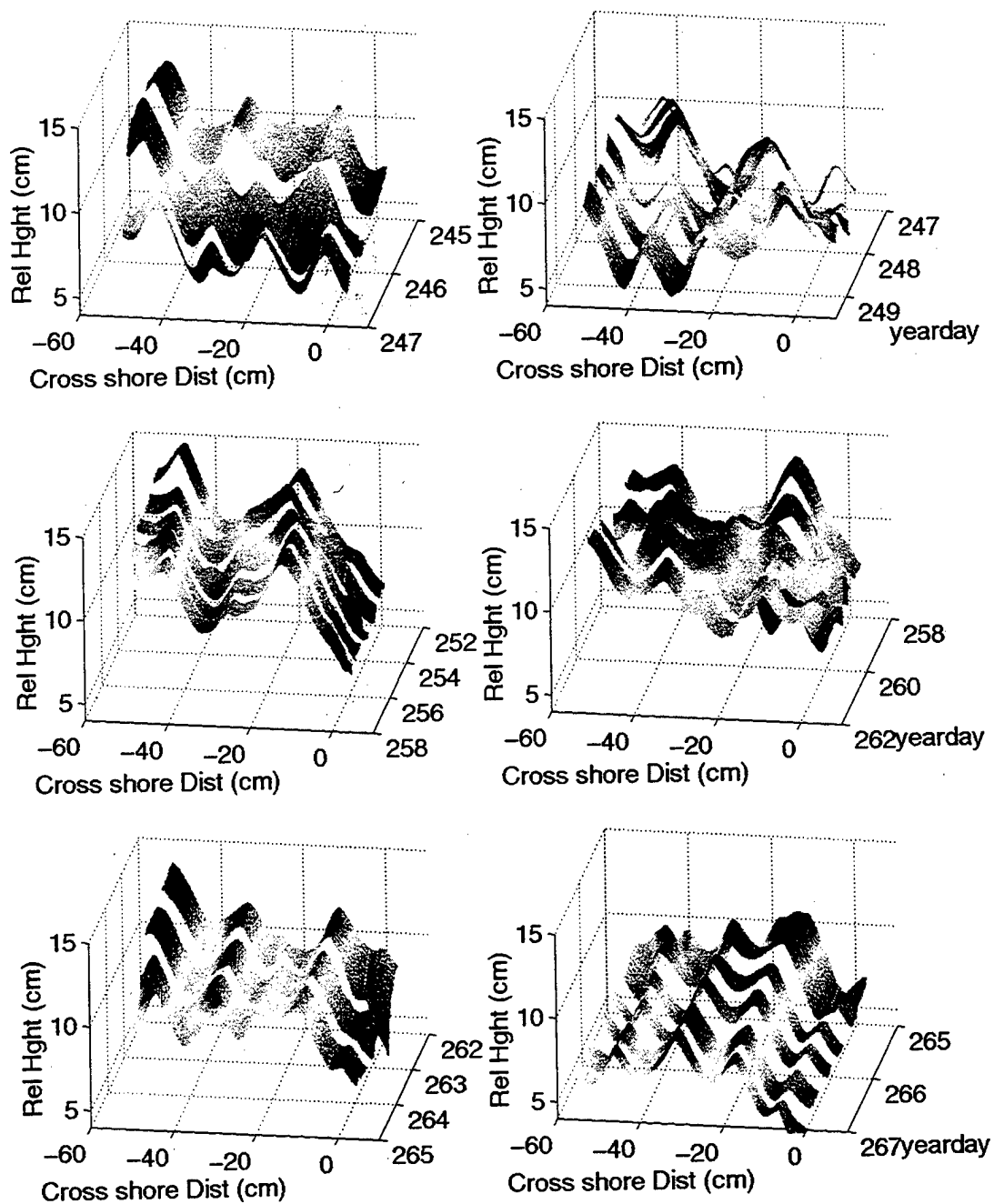
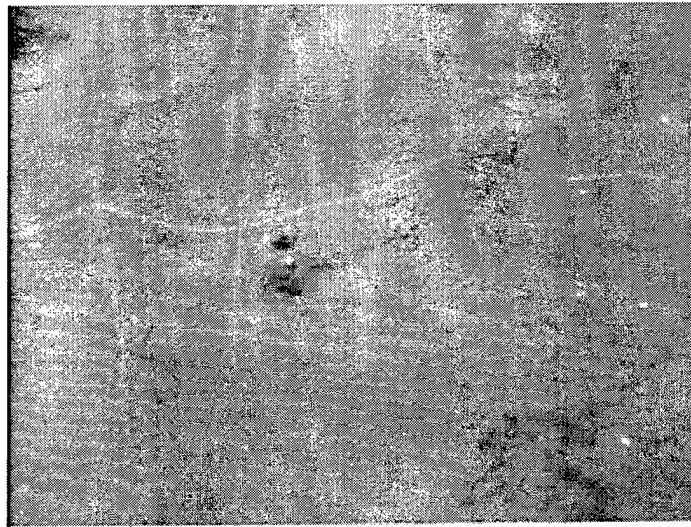


Figure 9. Time evolution of ripple geometries displayed in 3-4 day periods of relative ripple height (grayscale) vs. cross-shore distance (positive is offshore).

min 00:50:19 09/10/-1

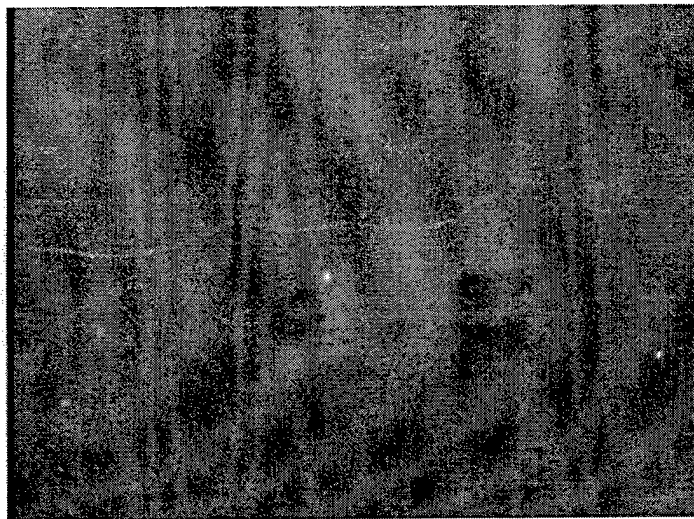


Onshore

Cross Shore

offshore

mean 00:00:19 09/18/-1



Onshore

Cross Shore

offshore

Figure 10a. Raw image of long crested ripples on yearday 253 (9/10/99) evolve into shorter bifurcated ripples (Figure 10b) on yearday 261 (9/18/99). The long crested two are left after the strong forcing on yearday 249-252. These give way after the high waves on yearday 259-261 to a short crested bifurcation.

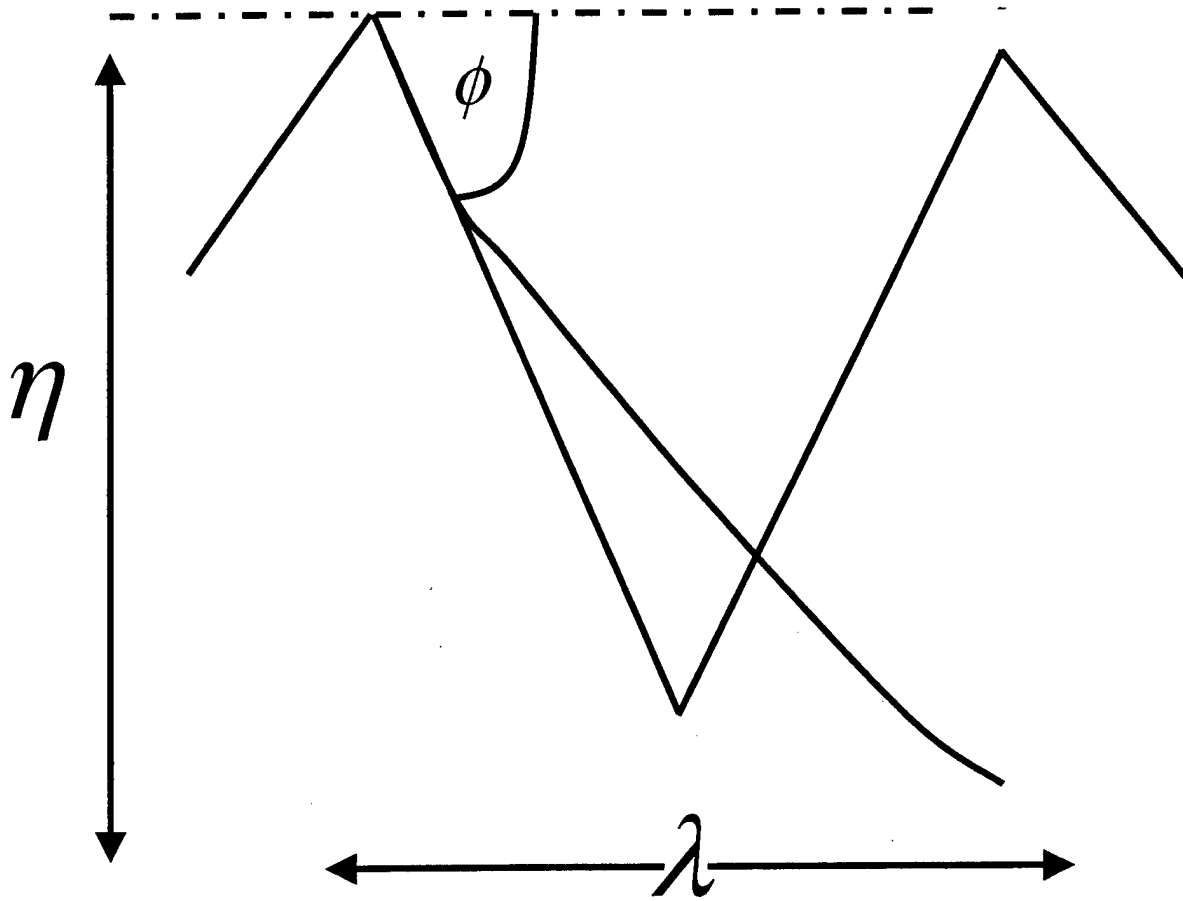


Figure 11. With maximum slope on the ripple profile is equal to  $\tan \phi$ , the height to length ratio must for geometric reasons be  $0.5 \tan \phi$  for a triangle ripple and  $0.25 \tan \phi$  for a parabolic ripple (after Nielsen 1992).



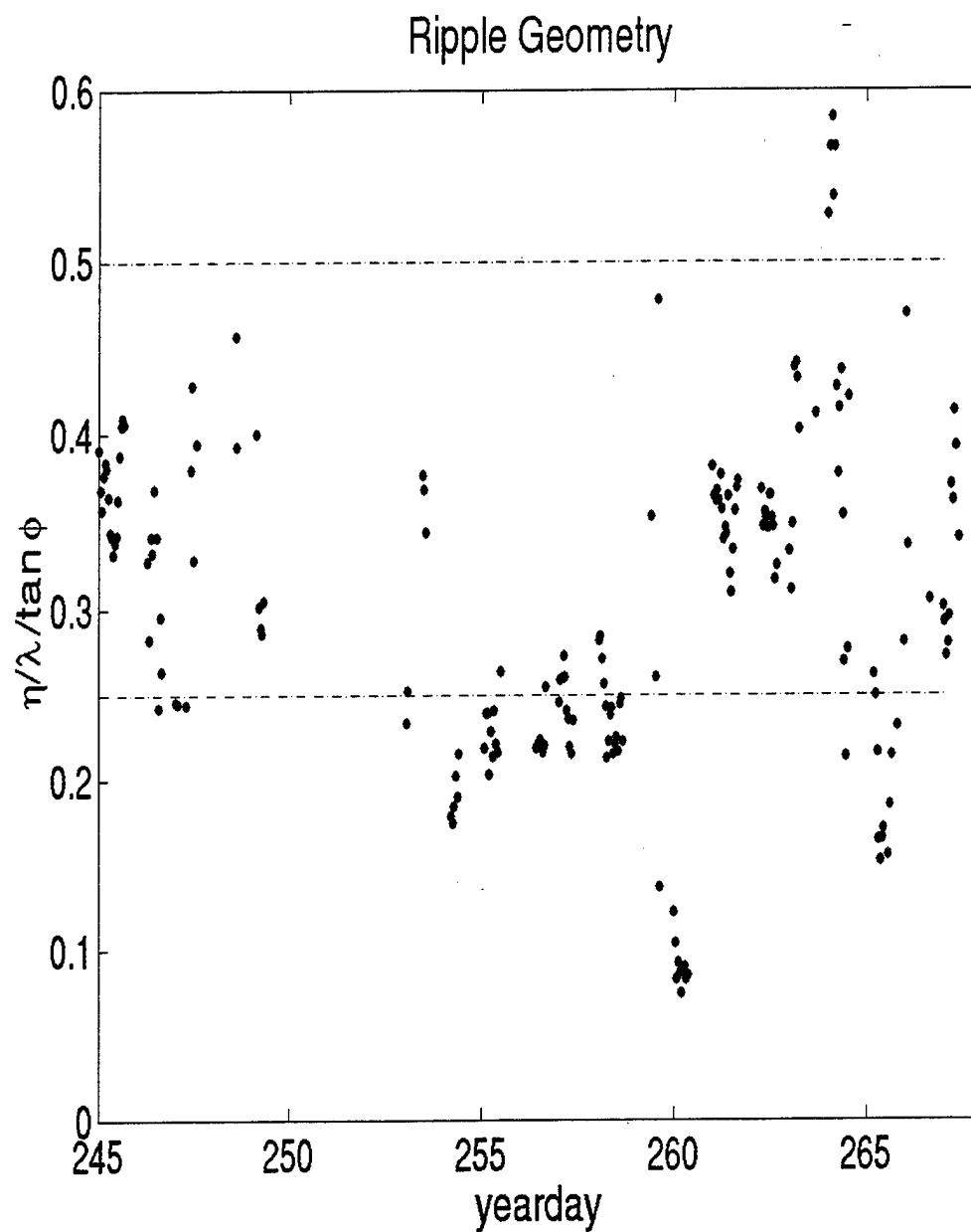


Figure 12. Time series of ripple steepness/ $\tan \phi$ . Bed slope geometry data generally falls between  $0.25 < \frac{\eta/\lambda}{\tan \phi} < 0.5$ .  $\frac{\eta/\lambda}{\tan \phi} < 0.25$  when  $\theta_{crit}$  is not exceeded.

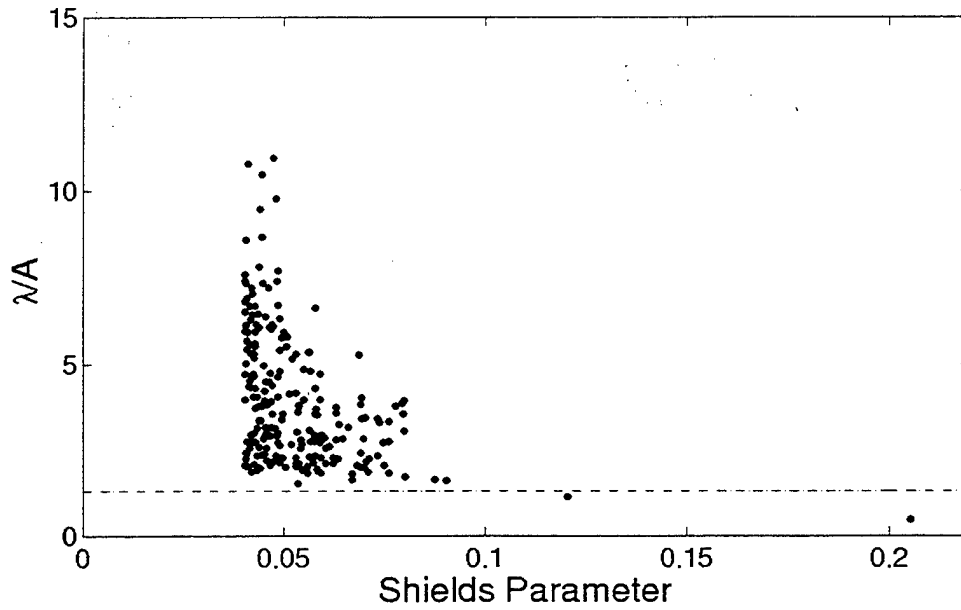
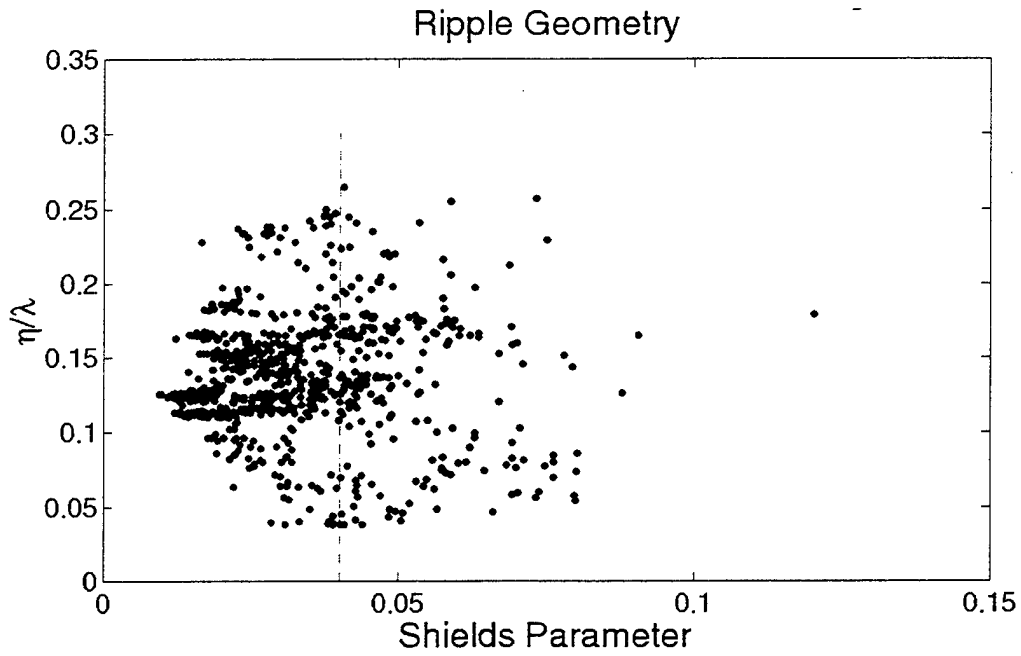


Figure 13a. Ripple steepness is highly variable. Figure 13b. Relative ripple length parameterized by orbital excursion (plotted only when  $\theta > \theta_{crit}$ ) decreases as forcing and orbital excursion increases. The dashed line corresponds to  $\lambda \approx 1.3\Lambda$ .

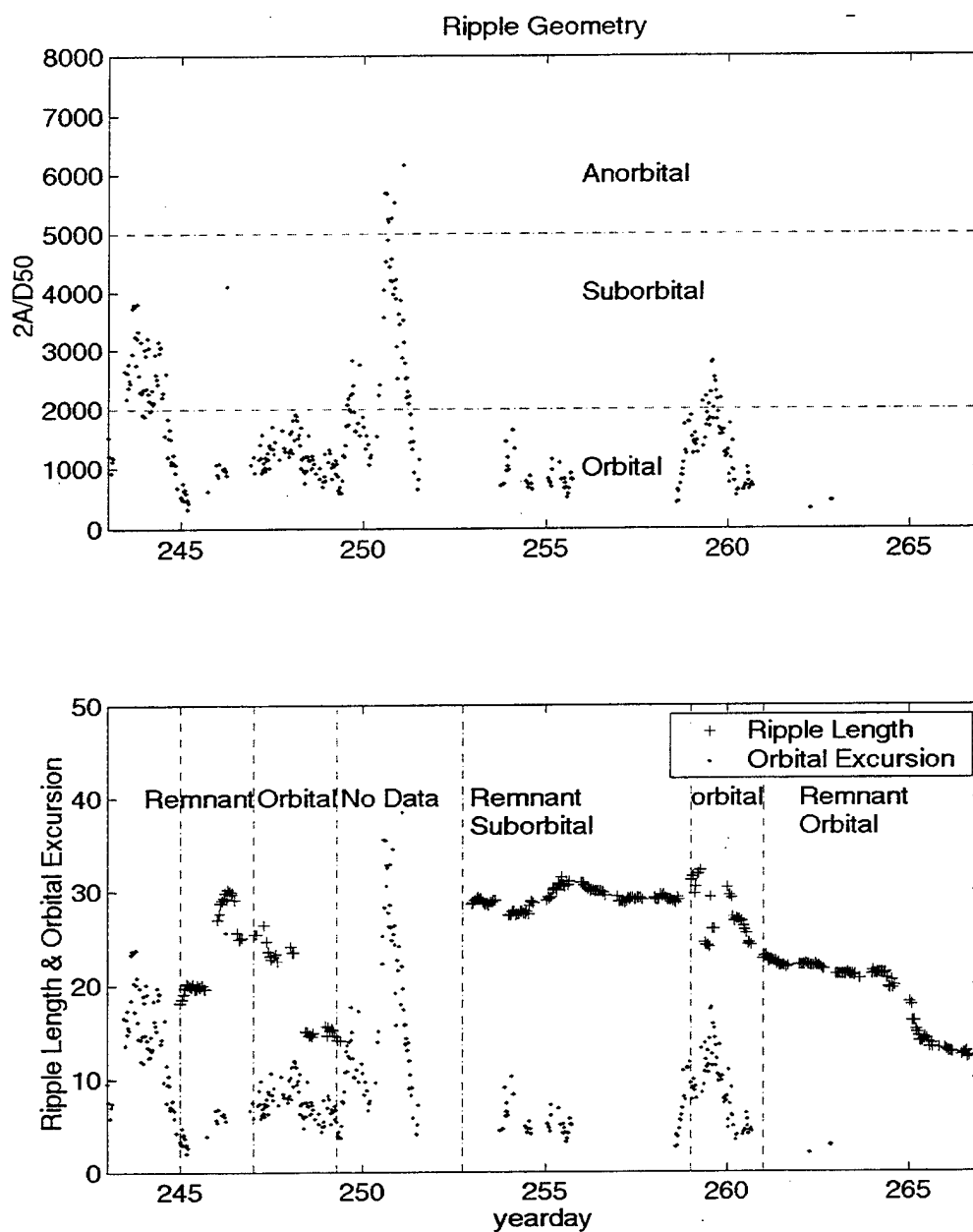


Figure 14a. Ripple Geometry (Clifton and Dingler, 1976) classified into orbital,  $(2A/d_{50}) < 2000$ , suborbital,  $2000 < 2A/d_{50} < 5000$ , and, anorbital,  $2A/d_{50} > 5000$ . Figure 14b. Time series of  $\lambda$  and  $A$ . Only values of  $A$  have been plotted when  $\theta > \theta_{crit}$ .

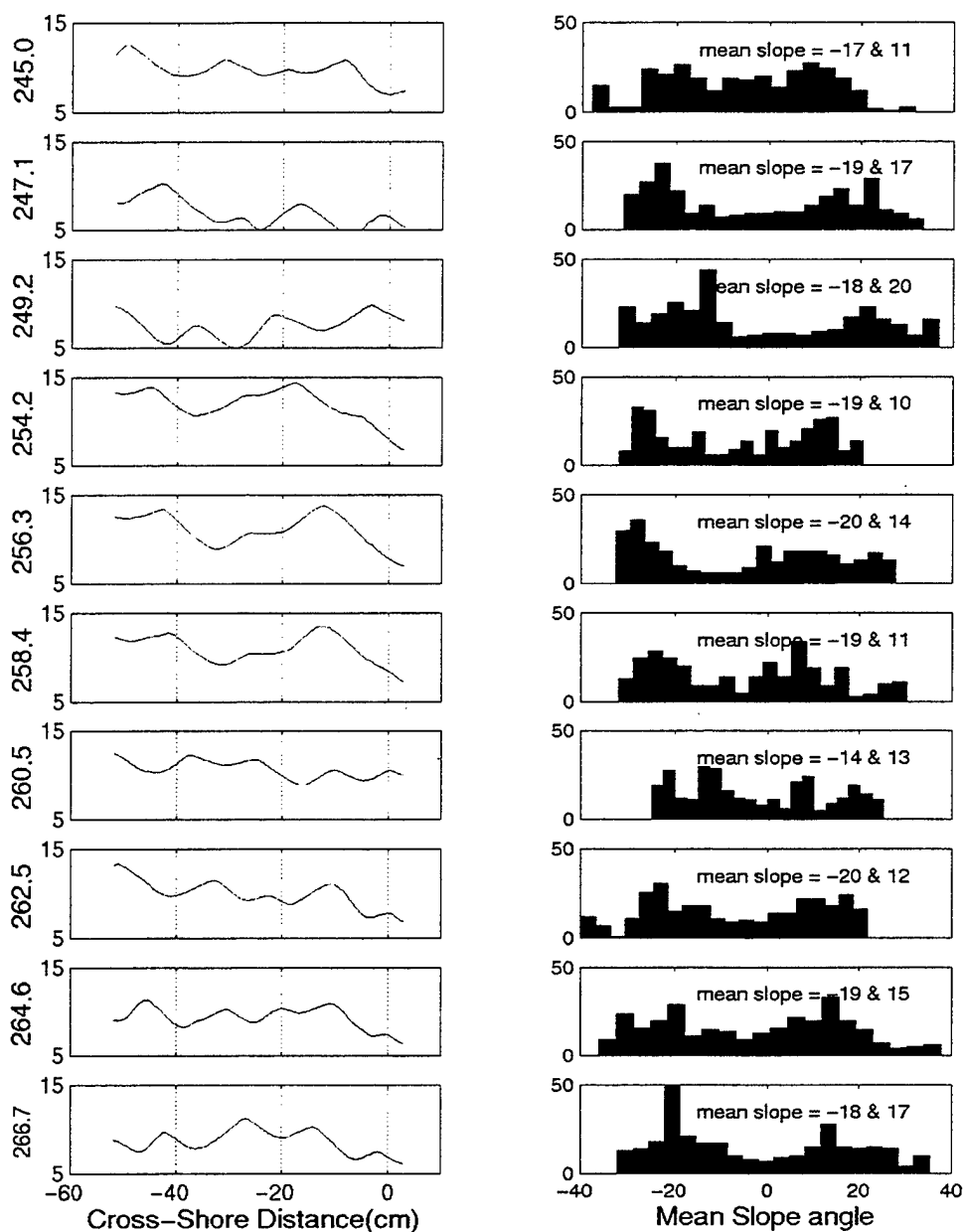


Figure 15. Left panel show evolution of selected images of cross-shore distance (positive is offshore) vs relative ripple height. Right panel shows histogram of slope angle with mean slope angle displayed above histogram. Mean slope angles were calculated by averaging the slope angle between crest and succeeding trough. The negative slopes angle are the mean slopes on the off shore side, while the positive slope angle are the slope angles on the onshore side.

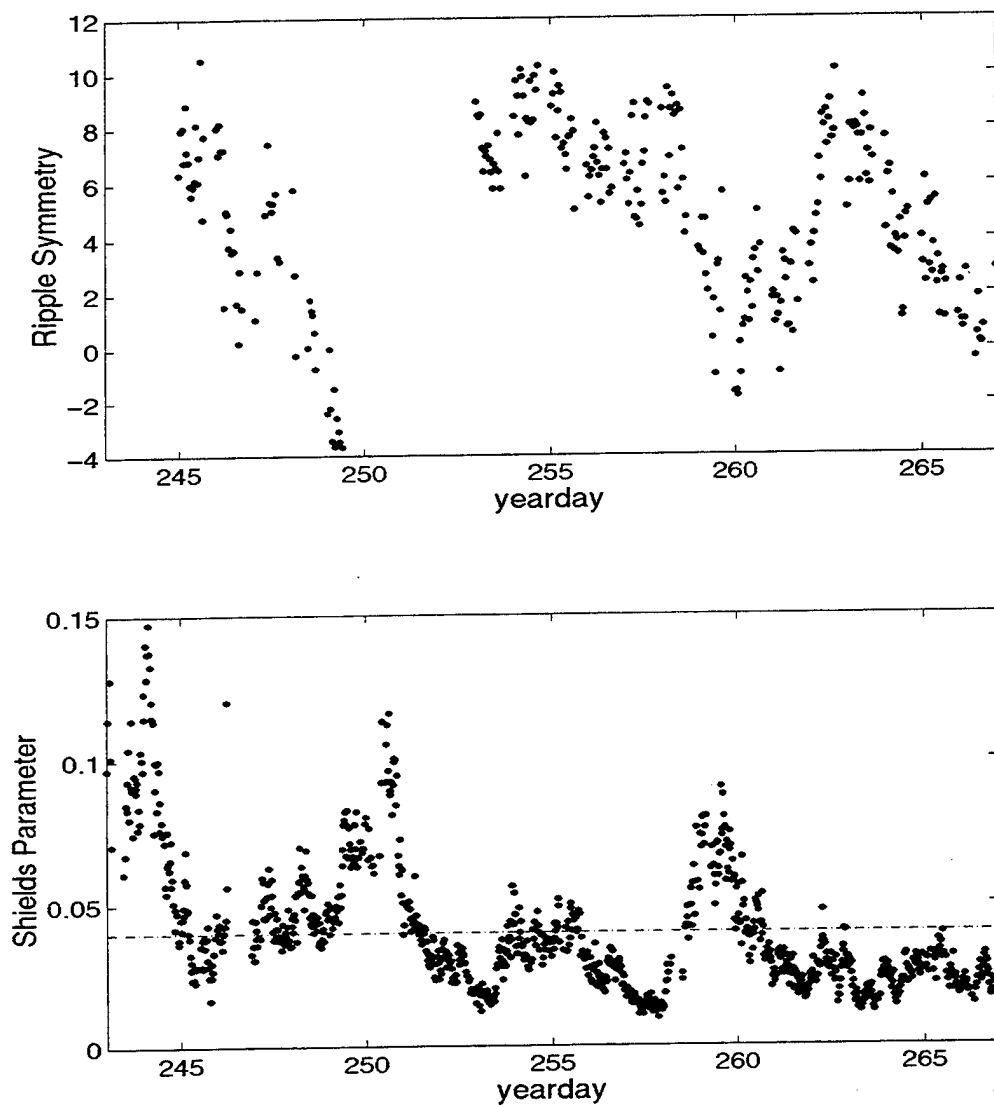


Figure 16a. Ripple Asymmetry: Large positive values show steeper sloping ripples on the off-shore side indicative of offshore migration while small values show symmetric ripples. Negative values show steeper sloping ripples on the on-shore side. Asymmetric ripples were left after strong wave forcing (high value of Shields Parameter, Figure 16b) and tended toward symmetry as the forcing subsided.

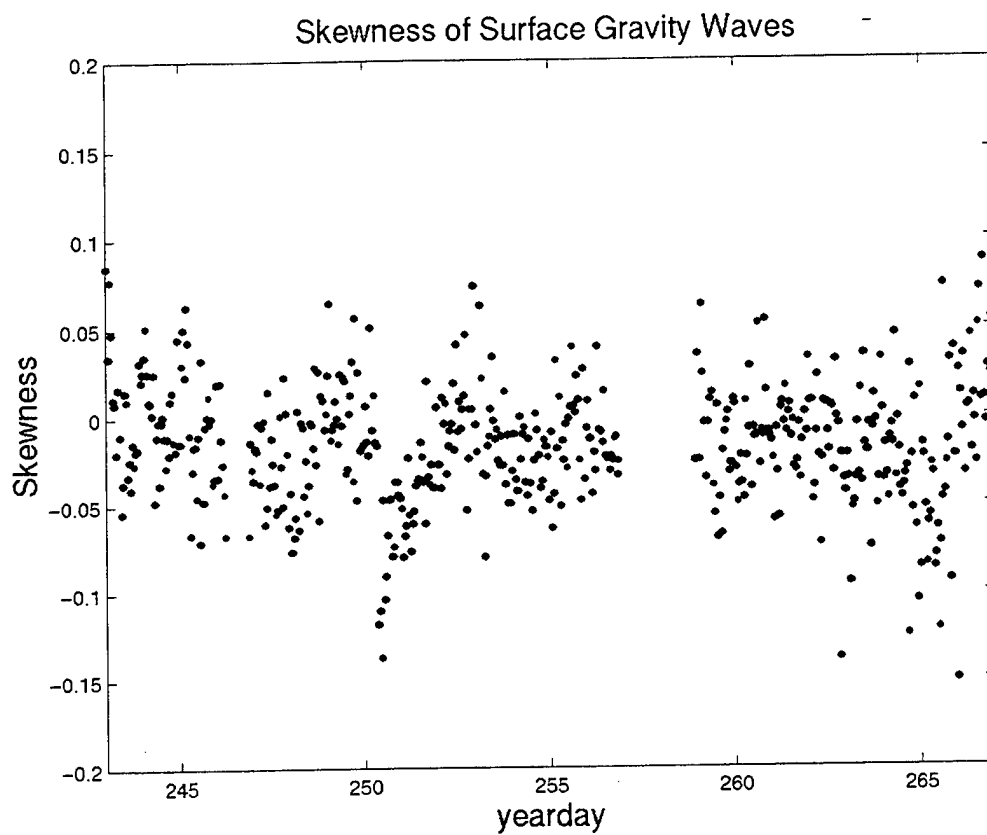


Figure 17. Skewness of cross-shore orbital velocity from surface gravity waves. A high pass filter at 0.05 Hz was applied to the cross-shore velocity time series and skewness values were calculated over one-hour samples.

# BOUND LONG WAVE THEORY

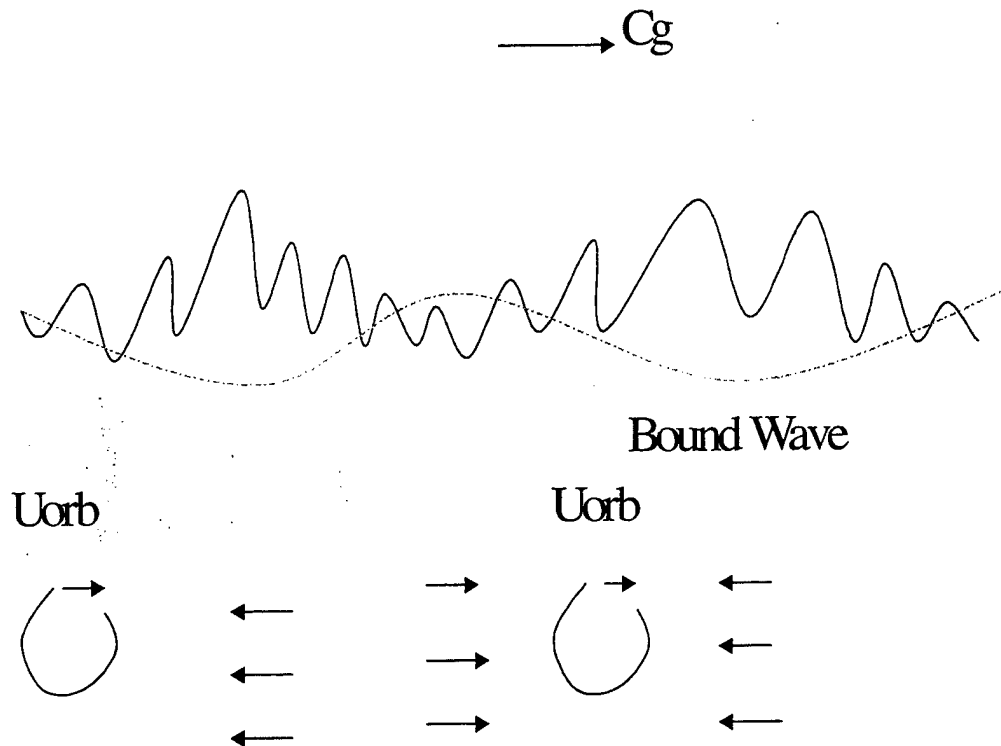


Figure 18. Change in momentum (high waves) is balanced by set down of forced long wave and small waves is balanced by a relative set-up. The forced long wave gives reverse flow under high wave and forward flow under small waves. Because more sediment is suspended during the larger waves. Net transport is reversed or offshore.

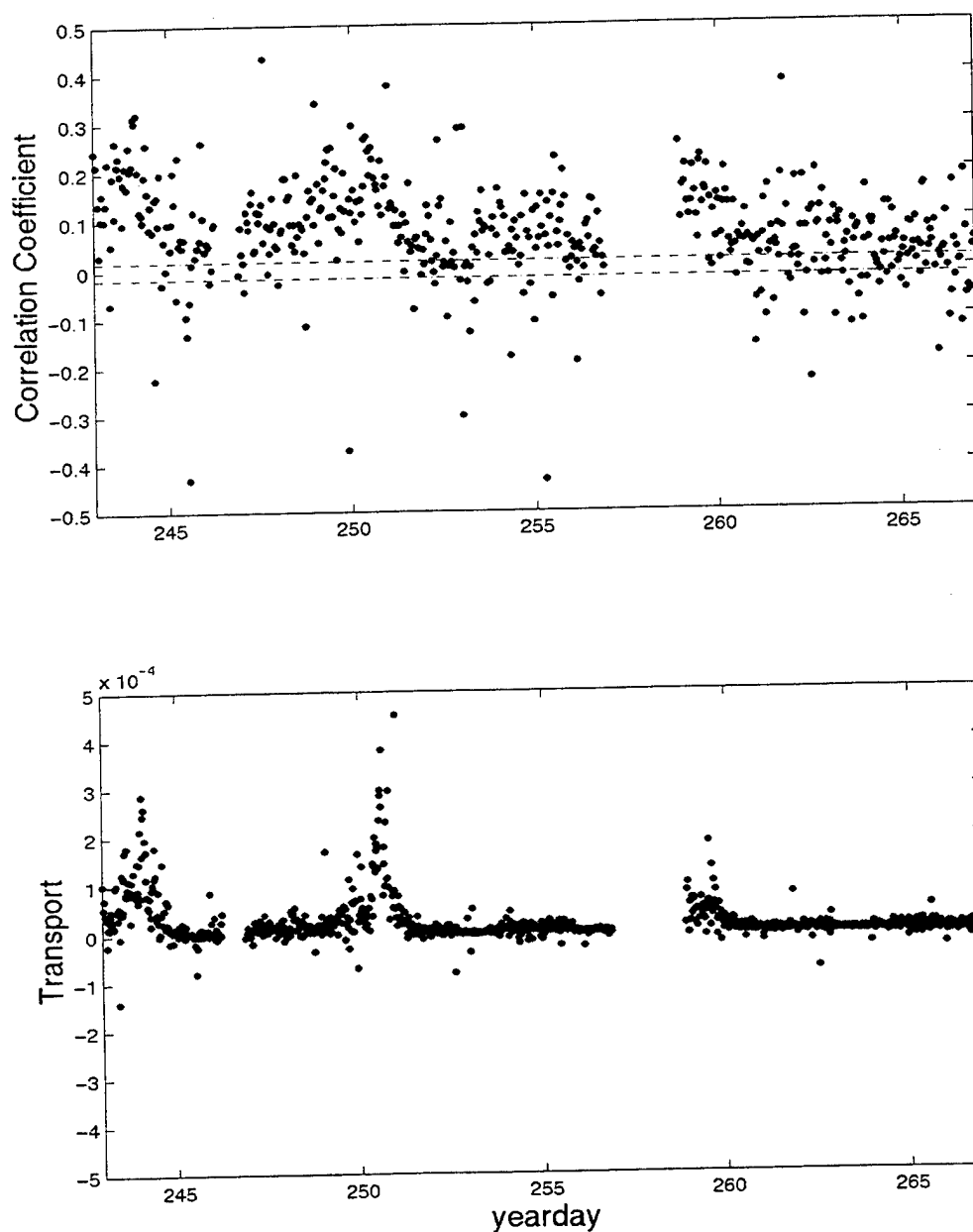


Figure 19a. Correlation Coefficient determined by correlating the infragravity wave band (obtained by low pass filtering the cross-shore velocity at 0.05 Hz) with the envelope of the sea-swell band of frequencies. The dashed lines represent the significant correlation. Figure 19b. Correlation as calculated in (a), but is not normalized. Correlation is determined by  $u_{lp} * (u^2)_{lp}$ .



THIS PAGE INTENTIONALLY LEFT BLANK

## LIST OF REFERENCES

- Amos, C.L., Bowen, A.J., Huntley, D.A., and Lewis, C.F.M., Ripple Generation Under the Combined Influences of Waves and Currents on the Canadian Continental Shelf. *Cont. Shelf Res.*, 8, 1129-1153, 1988.
- Andersen, K.H., The Dynamics of Ripples Beneath Surface Waves and Topics in Shell Models of Turbulence, PH. D. dissertation, University of Copenhagen, 142, pp., 1999.
- Bagnold, R.A., Motions of Waves in Shallow Water; Interaction Between Waves and Sand Bottoms, *Proc. R. Soc. London, Ser. A*, 187, 1-15, 1946.
- Boyd, R., D.L. Forbes, and D.E. Heffler, Time-Sequence Observations of Wave-Formed Sand Ripples on an Ocean Shoreface, *Sedimentology*, 35, 449-464, 1988.
- Clifton, H.E., and J.R. Dingler, Wave-formed Sedimentary Structures and Paleoenvironmental Reconstruction, *Mar. Geol.*, 60, 165-198, 1984.
- Crawford, A.M., and A.E. Hay, A Simple System for Laser-illuminated Video Imaging of Sediment Suspension and Bed Topography, *IEEE J. of Ocean. Eng.*, 23(1), 12-19, 1998.
- Deigaard, R., J.B. Jakobsen, and J. Fredsoe, Net Sediment Transport Under Wave Groups and Bound Long Waves, *J. of Geophys. Res.*, 104 (C6), 13559-13575, 1999.
- Engelund, F., and J. Fredsoe, Sediment Ripples and Dunes, *Annu. Rev. Fluid Mech.*, 14, 13-37, 1982.
- Fredsoe, J., and R. Deigaard, *Mechanics of Coastal Sediment Transport*, World Sci., River Edge, N.J., 1992.
- Grant, W.D., and O.S. Madsen, Quantitative Description of Sediment Transport by Waves, *Proc. 15<sup>th</sup> Int. Conf. On Coastal Engineering*, Honolulu ASCE, 1093-1112, 1976.
- Hanes, D.M., Suspension of Sand Due to Wave Groups, *J. Geophys. Res.*, 96 (C5), 8911-8915, 1991.
- Hay, A.E., and D.J. Wilson, Rotary Sidescan Images of Nearshore Bedform Evolution During a Storm, *Mar. Geol.*, 119, 57-65, 1994.
- Inman, D.L., and A.J. Bowen, Flume Experiments on Sand Transport by Waves and Currents, in *Coastal Engineering, Proceedings of the 8<sup>th</sup> Conference*, pp. 137-150, Am. Soc. Civ. Eng., New York, 1963.

Longuet-Higgins, M.S., and R. W. Stewart, Radiation Stress in Water Waves: A Physical Discussion with Applications, *Deep Sea Res.*, 111, 529-562, 1964.

Nielsen, P., Some Basic Concepts of Wave Sediment Transport, Ser. Paper 20 Inst Hydrodyn Hydraul Eng, Tech Univ Denmark, 160 pp., 1979.

Nielsen, P., Dynamics and Geometry of Wave Generated Ripples, *J. Geophys. Res.*, 86, C7, 6467-6472, 1981.

Nielsen, P. *Coastal bottom Boundary Layers and Sediment Transport*, World Scientific, 1992.

Shi, N. C., and L.H. Larsen, Reverse Sediment Transport Induced by Amplitude Modulated Waves, *Mar Geol.*, 54, 181-200, 1984.

Swart, D. H., Offshore Sediment Transport and Equilibrium Beach Profiles, *Delft Hydr Lab Publ*, 131, 1974.

Stanton, T.P., [WWW.oc.nps.navy.mil/~stanton/miso](http://WWW.oc.nps.navy.mil/~stanton/miso)

Tanaka. H., and Shuto, N., Sand Movement Due to Wave-current Combined Motion. *Coast. Engrg. in Japan*, Tokyo, 27, 179-191, 1984.

Traykovski, Peter, A.E. Hay, J.D. Irish, and J.F. Lynch, Geometry, Migration and Evolution of Wave Orbital Ripples at LEO-15, *J. Geophys. Res.*, 104, C1, 1505-1524, 1999.

## INITIAL DISTRIBUTION LIST

	No. Copies
1. Defense Technical Information Center..... 8725 John J. Kingman Rd, STE 0944 Ft. Belvoir, VA 22060-6218	2
2. Dudley Knox Library..... Naval Postgraduate School 411 Dyer Rd Monterey, CA 93943-5101	2
3. Chairman (Code OC/Gd)..... Department of Oceanography Naval Postgraduate School Monterey, CA 93943-5122	1
4. Chairman (Code MR/Wx)..... Department of Meteorology Naval Postgraduate School Monterey, CA 93943-5114	1
5. Dr. Edward B. Thornton, (Code OC/Tm)..... Department of Oceanography Naval Postgraduate School Monterey, CA 93943-5122	2
6. Professor Tim Stanton, (Code OC/St) ..... Department of Oceanography Naval Postgraduate School Monterey, CA 93943-5122	2
7. Damon Dixon ..... 704 San Gabriel Place Chula Vista, CA 91914	4
8. Lori Boettler ..... 16 Greenwood Court Orinda, CA 94563	1
9. Cameron Hansen ..... 7693 Summerhill Court Salt Lake City, UT 84121	1